

# High-resolution U.S. methane emissions inferred from an inversion of 2019 TROPOMI satellite data: contributions from individual states, urban areas, and landfills

Hannah Nesser<sup>1\*</sup>, Daniel J. Jacob<sup>1</sup>, Joannes D. Maasakkers<sup>2</sup>, Alba Lorente<sup>2</sup>, Zichong Chen<sup>1</sup>, Xiao Lu<sup>3</sup>, Lu Shen<sup>4</sup>, Zhen Qu<sup>5</sup>, Melissa P. Sulprizio<sup>1</sup>, Margaux Winter<sup>1</sup>, Shuang Ma<sup>6</sup>, A. Anthony Bloom<sup>6</sup>, John R. Worden<sup>6</sup>, Robert N. Stavins<sup>7</sup>, Cynthia A. Randles<sup>8†</sup>

<sup>1</sup>School of Engineering and Applied Sciences, Harvard University, Cambridge, MA, USA

<sup>2</sup>SRON Netherlands Institute for Space Research, Leiden, the Netherlands

<sup>3</sup>School of Atmospheric Sciences, Sun Yat-sen University, Zhuhai, Guangdong Province, China

<sup>4</sup>Department of Atmospheric and Oceanic Sciences, School of Physics, Peking University, Beijing, China

<sup>5</sup>Department of Marine, Earth and Atmospheric Sciences, North Carolina State University, Raleigh, NC, USA

<sup>6</sup>Jet Propulsion Laboratory, California Institute of Technology, Pasadena, California, USA

<sup>7</sup>Harvard Kennedy School, Cambridge, MA, USA

<sup>8</sup>ExxonMobil Technology and Engineering Company, Annandale, NJ, USA

<sup>15</sup>\*Now at Jet Propulsion Laboratory, California Institute of Technology, Pasadena, California, USA

<sup>†</sup>Now at United Nations Environment Program International Methane Emissions Observatory, Paris, France

*Correspondence to:* Hannah Nesser (hannah.o.nesser@jpl.nasa.gov)

**Abstract.** We quantify 2019 annual mean methane emissions in the contiguous U.S. (CONUS) at  $0.25^\circ \times 0.3125^\circ$  resolution by inverse analysis of atmospheric methane columns measured by the Tropospheric Monitoring Instrument (TROPOMI). A gridded version of the U.S. Environmental Protection Agency (EPA) Greenhouse Gas Emissions Inventory (GHGI) serves as the basis for the prior estimate for the inversion. We optimize emissions and quantify observing system information content for an eight-member inversion ensemble through analytical minimization of a Bayesian cost function. We achieve high resolution with a reduced-rank characterization of the observing system that optimally preserves information content. Our optimal (posterior) estimate of anthropogenic emissions in CONUS is  $30.9$  ( $30.0 - 31.8$ )  $\text{Tg a}^{-1}$ , where the values in parentheses give the spread of the ensemble. This is a 13% increase from the 2023 GHGI estimate for CONUS in 2019. We find livestock emissions of  $10.4$  ( $10.0 - 10.7$ )  $\text{Tg a}^{-1}$ , oil and gas of  $10.4$  ( $10.1 - 10.7$ )  $\text{Tg a}^{-1}$ , coal of  $1.5$  ( $1.2 - 1.9$ )  $\text{Tg a}^{-1}$ , landfills of  $6.9$  ( $6.4 - 7.5$ )  $\text{Tg a}^{-1}$ , wastewater of  $0.6$  ( $0.5 - 0.7$ ), and other anthropogenic sources of  $1.1$  ( $1.0 - 1.2$ )  $\text{Tg a}^{-1}$ . The largest increase relative to the GHGI occurs for landfills (51%), with smaller increases for oil and gas (12%) and livestock (11%). These three sectors are responsible for 89% of posterior anthropogenic emissions in CONUS. The largest decrease (28%) is for coal. We exploit the high resolution of our inversion to quantify emissions from 70 individual landfills, where we find emissions are on median 77% larger than the values reported to the EPA's Greenhouse Gas Reporting Program (GHGRP), a key data source for the GHGI. We attribute this underestimate to overestimated recovery efficiencies at landfill gas facilities and to under-accounting of site-specific operational changes and leaks. We also quantify emissions for the 48 individual states in CONUS, which we compare to the GHGI's new state-level inventories and to independent state-produced inventories. Our posterior emissions are on average 27% larger than the GHGI in the largest 10 methane-producing states, with the biggest upward adjustments in

states with large oil and gas emissions, including Texas, New Mexico, Louisiana, and Oklahoma. We also calculate emissions for 95 geographically diverse urban areas in CONUS. Emissions for these urban areas total 6.0 (5.4 - 6.7) Tg a<sup>-1</sup> and are on average 39 (27 - 52) % larger than a gridded version of the 2023 GHGI, which we attribute to underestimated landfill and gas distribution emissions.

## 40 1 Introduction

All projected pathways that prevent global warming above 1.5°C require methane emissions reductions (IPCC, 2022). The Global Methane Pledge, launched at a 2021 meeting of the United Nations Framework Convention on Climate Change (UNFCCC), aims to achieve a 30% global reduction in methane emissions from 2020 to 2030 (About the Global Methane Pledge, 2023). Consistent with that goal, the U.S. government is targeting methane emission decreases from oil and gas, 45 livestock, and landfills (The White House, 2021). The UNFCCC requires member parties to report their anthropogenic methane emissions including sectoral contributions from oil and gas, coal, livestock, rice, landfills, and wastewater. The bottom-up approaches used to generate these emission inventories use information on sectoral activity levels and emission factors, but considerable uncertainty can exist in these values. Top-down evaluations of bottom-up inventories use observations of atmospheric methane to infer emissions, often through inverse analyses using a chemical transport model. These top-down 50 emission estimates are most useful for the evaluation of emission inventories and emission mitigation efforts if they achieve high spatial resolution consistent with the information content of the observation-model system. Here we use column methane observations from the Tropospheric Monitoring Instrument (TROPOMI) aboard the Sentinel-5 Precursor satellite in a reduced-rank analytical inversion to infer methane emissions and the associated information content at 0.25° × 0.3125° ( $\approx$ 25 km × 25 km) resolution over the contiguous U.S. (CONUS) for 2019, allowing for detailed analysis of sectoral, state, and urban 55 emissions.

Satellite observations of atmospheric methane column concentrations inferred from measurement of backscattered sunlight in the shortwave infrared have been used extensively in inverse analyses of methane emissions (Streets et al., 2013; Jacob et al., 2022). Previous satellite instruments were limited by large pixel sizes (SCIAMACHY, 2003 - 2012) or sparse observations 60 (GOSAT, 2009 - present). TROPOMI provides daily, global observations of atmospheric methane columns at 5.5 km × 7 km nadir pixel resolution (Hu et al., 2018) with a ~3% success rate limited by cloud cover, optically dark surfaces, and heterogeneous terrain (Hasekamp et al., 2019). Inversions of TROPOMI data allow for high-resolution quantification of methane emissions but require understanding the information content of the observations.

65 Inverse analyses optimize methane emissions (the state vector) by fitting observations to simulated concentrations from a chemical transport model (CTM) that serves as the inversion forward model. The optimization is typically done by minimizing a Bayesian cost function regularized by a prior emission estimate given by a bottom-up inventory. When a linear relationship

exists between emissions and concentrations, as in the case of methane, the optimal (posterior) solution and the associated error covariances and information content can be found analytically (Brasseur and Jacob, 2017). However, this requires the  
70 computationally expensive but embarrassingly parallel construction of the Jacobian matrix that represents the relationship between emissions and concentrations in the CTM. This matrix is typically constructed by conducting a CTM perturbation simulation for each optimized emission element, limiting either the spatial resolution of the optimized emissions or the size of the inversion domain. Nesser et al. (2021) demonstrated an alternative method that approximates the Jacobian matrix by perturbing emission patterns that are optimally informed by both the prior emissions and the observations. This approach  
75 optimally exploits the information content of the observations, quantifying emissions at the highest resolution possible where the satellite-model observing system provides a constraint and defaulting to the prior estimate elsewhere.

Many inverse studies that quantified U.S. methane emissions using surface, aircraft, or satellite observations have found large discrepancies with the U.S. Environmental Protection Agency's (EPA) Greenhouse Gas Emissions Inventory (GHGI), which  
80 is the bottom-up emission estimate reported by the U.S. to the UNFCCC (EPA, 2023a). Wecht et al. (2014a) found livestock emissions 40% larger than the GHGI for the summer of 2004. Miller et al. (2013) inferred emissions 50% larger than the GHGI for 2007 and 2008, which they attributed to underestimated oil, gas, and livestock emissions. Turner et al. (2015) found similar results for 2009 to 2011. Maasakers et al. (2021) inferred oil and gas emissions 35% and 22% higher than the GHGI, respectively, for 2010 to 2015. Lu et al. (2022) found mean 2010 - 2017 anthropogenic emissions 42% larger than the GHGI,  
85 which they attributed largely to oil and gas emissions.

Higher resolution regional studies have targeted specific aspects of U.S. methane emissions, including contributions from different sectors, states, and urban areas. Karion et al. (2015) found oil and gas emissions in the Barnett Shale in eastern Texas that were consistent with the GHGI when scaled by the region's relative contribution to national gas production but larger than  
90 reported by most basin facilities to the EPA's Greenhouse Gas Reporting Program (GHGRP). A series of studies inferred much higher emissions in the Permian Basin than implied by a spatially allocated (gridded) version of the GHGI (Zhang et al., 2020; Schneising et al., 2020; Liu et al., 2021; Y. Chen et al., 2022; Varon et al., 2022). Z. Chen et al. (2018) and Yu et al. (2021) found underestimated livestock emissions in the gridded GHGI in the upper Midwest. Jeong et al. (2016) inferred California emissions 20% to 80% larger than a state inventory from the California Air Resources Board (CARB). Plant et al. (2019) found  
95 methane emissions from six East Coast urban areas in 2012 to be more than two times larger than the gridded GHGI.

Here we use the reduced-rank method of Nesser et al. (2021) in an analytical inversion of 2019 TROPOMI observations to quantify annual mean emissions at  $0.25^\circ \times 0.3125^\circ$  resolution over North America using national emission inventories reported by the U.S., Mexico, and Canada to the UNFCCC as prior estimates. The reduced-rank approach decreases computational cost  
100 by an order of magnitude compared to conventional methods while maximizing information content from TROPOMI. We focus our analysis on CONUS, with particular attention to emissions from individual landfills, states, and urban areas. We

compare our results to the 2023 GHGI, including estimates for individual states (EPA, 2023a, b). Our inversion provides the first observational evaluation for these state inventories. We also compare our results to inventories prepared by individual states and cities.

## 105 2 Data and methods

We conduct an ensemble of inversions of 2019 TROPOMI methane observations over the North American domain shown in Fig. 1 ( $9.75^{\circ}\text{N}$  -  $60^{\circ}\text{N}$ ,  $130^{\circ}\text{W}$  -  $60^{\circ}\text{W}$ ) using the nested GEOS-Chem CTM at  $0.25^{\circ} \times 0.3125^{\circ}$  resolution as forward model.

The  $m = 2919358$  TROPOMI observations are fit to simulated GEOS-Chem concentrations to optimize annual mean methane emissions for 2019 at the  $0.25^{\circ} \times 0.3125^{\circ}$  GEOS-Chem resolution. This corresponds to  $n = 23691$  emission grid cells with prior methane emissions larger than  $0.1 \text{ Mg km}^{-2} \text{ a}^{-1}$ , accounting for over 99% of North American methane emissions. In a subset of the ensemble, we optimize boundary conditions for the nested GEOS-Chem simulation for each of the four cardinal directions (north, south, east, and west). Methane chemical and soil sinks are not optimized because they are relatively small compared to emissions.

### 2.1 Reduced-rank analytical inversion

115 The inversion uses  $m$  observed concentrations arranged in a vector  $\mathbf{y}$  to optimize  $n$  gridded emissions arranged in the state vector  $\mathbf{x}$  by minimizing a Bayesian cost function  $J$  assuming normal errors and regularized by the prior emission estimate  $\mathbf{x}_A$  (Rodgers, 2000):

$$J(\mathbf{x}) = (\mathbf{x} - \mathbf{x}_A)^T \mathbf{S}_A^{-1} (\mathbf{x} - \mathbf{x}_A) + \gamma (\mathbf{y} - \mathbf{Kx})^T \mathbf{S}_0^{-1} (\mathbf{y} - \mathbf{Kx}). \quad (1)$$

120

The prior and observing system error covariance matrices  $\mathbf{S}_A$  and  $\mathbf{S}_0$ , respectively, are assumed diagonal in the absence of better information. The regularization factor  $\gamma$  corrects for the absence of covariance in  $\mathbf{S}_0$  (Chevallier, 2007). We generate an eight-member inversion ensemble using a range of prior error variances and  $\gamma$  values to capture the inversion's sensitivity to uncertainty in these parameters (Sect. 2.7). The reduced-rank Jacobian matrix  $\mathbf{K} = \partial\mathbf{y}/\partial\mathbf{x}$  represents the sensitivity of concentrations to emissions in the CTM. We construct a rank- $k$  Jacobian matrix for the  $0.25^{\circ} \times 0.3125^{\circ}$  GEOS-Chem grid by perturbing in the CTM the  $k$  emission patterns that best capture the prior emissions and the information content of the TROPOMI observations (Sect. 2.6).

130 Analytical minimization of the cost function following Rodgers (2000) yields the optimal (posterior) state vector estimate  $\hat{\mathbf{x}}$ , error covariance matrix  $\hat{\mathbf{S}}$ , and information content given by the averaging kernel matrix  $\mathbf{A} = \partial\hat{\mathbf{x}}/\partial\mathbf{x} = \mathbf{I} - \hat{\mathbf{S}}\mathbf{S}_A^{-1}$ , which describes the sensitivity of the posterior estimate to the true state vector. However, this solution requires inverting the cost function Hessian, which produces numerical instabilities due to the rank reduction of the Jacobian matrix. Here we use a

reduced-rank approximation of the posterior solution following Bousserez and Henze (2018) to solve the inversion on an orthonormal basis that optimally spans the information content of the satellite–forward model observing system. The basis is given by the eigendecomposition of the prior-preconditioned Hessian of the cost function,

$$\hat{\mathbf{H}}_p = \mathbf{S}_A^{1/2} \mathbf{K}^T \mathbf{S}_0^{-1} \mathbf{K} \mathbf{S}_A^{1/2} = \mathbf{V} \Lambda \mathbf{V}^T, \quad (2)$$

where the columns of  $\mathbf{V}$  are the eigenvectors and  $\Lambda$  is a diagonal matrix with entries equal to the eigenvalues. The calculation of  $\hat{\mathbf{H}}_p$  requires substantial memory for large  $m$  and  $n$ , for which we use Dask, a Python parallelization package (Dask Development Team, 2016). The reduced-rank posterior approximation is then generated using the largest  $k$  eigenvalues  $\Lambda_k$  and the associated eigenvectors  $\mathbf{V}_k$  (Bousserez and Henze, 2018):

$$\mathbf{A}_K = \gamma \mathbf{S}_A \mathbf{V}_k \Lambda_k (\mathbf{I}_k + \gamma \Lambda_k)^{-1} \mathbf{V}_k^T \mathbf{S}_A, \quad (3)$$

$$\hat{\mathbf{S}}_K = (\mathbf{I}_n - \mathbf{A}_K) \mathbf{S}_A, \text{ and} \quad (4)$$

$$\hat{\mathbf{x}}_{\text{FR}} = \mathbf{x}_A + \gamma \hat{\mathbf{S}}_K \mathbf{K}^T \mathbf{S}_0^{-1} (\mathbf{y} - \mathbf{F}(\mathbf{x}_A)). \quad (5)$$

145

Here,  $\hat{\mathbf{x}}_{\text{FR}}$  approximates the full-rank (FR) posterior  $\hat{\mathbf{x}}$  by minimizing the difference between the two, and  $\hat{\mathbf{S}}_K$  and  $\mathbf{A}_K$  are the optimal posterior error covariance and averaging kernel matrices, respectively, for an inversion solved with a reduced-rank forward model. We set  $k$  to match the rank of the reduced-rank Jacobian matrix, which is chosen to maximize information content within the available computational resources (Sect. 2.6). The diagonal elements of  $\mathbf{A}_k$  are often referred to as averaging kernel sensitivities and are a measure of the dependence of the optimized emissions on the prior estimate. Their sum (trace of  $\mathbf{A}_k$ ) gives the degrees of freedom for signal (DOFS) that represent the number of pieces of information independently quantified by the observing system (Rodgers, 2000). The reduced-rank inversion and Jacobian matrix do not attempt to optimize emissions in areas with low information content, so we default to the prior estimate for grid cells with averaging kernel sensitivities less than 0.05 (Nesser et al., 2021).

155

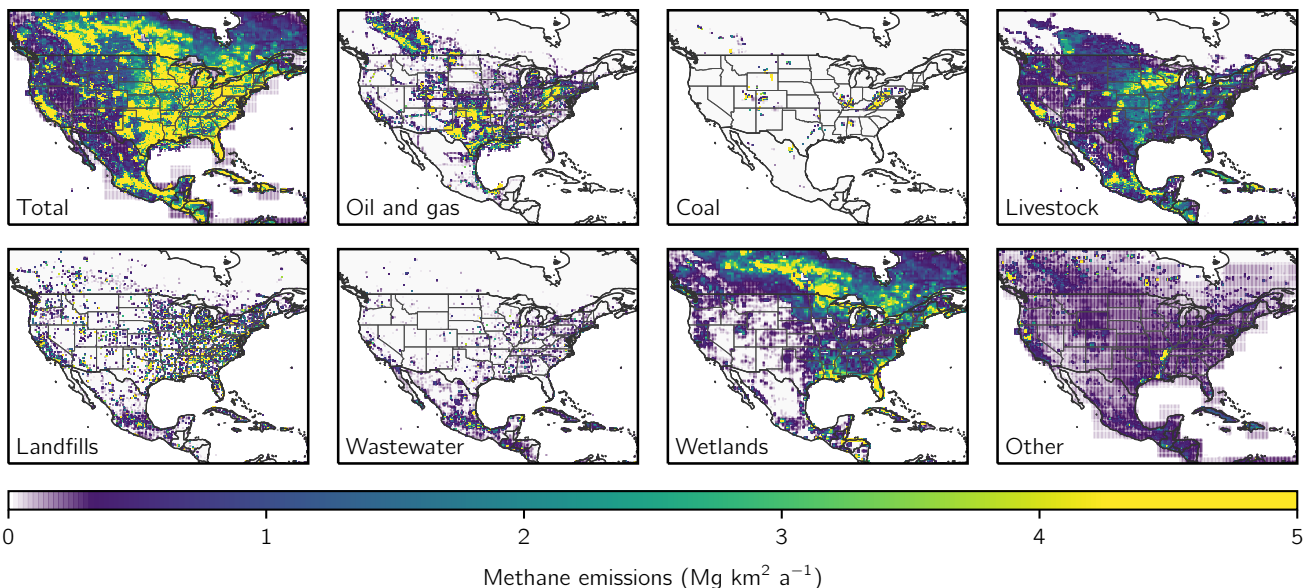
## 2.2 Prior estimates and errors

Figure 1 shows the annual-average prior emission estimates for different sectors. Anthropogenic emissions are given by the spatially disaggregated (gridded) versions of the 2016 EPA GHGI for the U.S. for 2012 (Maasakkers et al., 2016), the Instituto Nacional de Ecología y Cambio Climático (INECC) inventory for Mexico for 2015 (Scarpelli et al., 2020), and the Environment and Climate Change Canada (ECCC) inventory for Canada for 2018 (Scarpelli et al., 2021). We update the distribution and magnitude of GHGI oil and gas emissions to the 2020 GHGI for 2018 following Shen et al. (2022) and use the Environmental Defense Fund’s inventory for the Permian basin for 2019 (Zhang et al., 2020), where GHGI estimates are known to be too low (Zhang et al., 2020; Schneising et al., 2020; Liu et al., 2021; Y. Chen et al., 2022; Varon et al., 2022).

We treat oil and gas as a single sector in our analysis due to significant source co-location and uncertainty in the partitioning of oil and gas wells. The magnitude of GHGI livestock, landfill, and wastewater emissions changed by less than 10% from 165 2012 to 2019, while coal emissions decreased by 26%. The distribution of these sources is unlikely to have changed significantly. Anthropogenic emissions for Central America and the Caribbean islands are from the EDGAR v4.3.2 global emission inventory for 2012 (Janssens-Maenhout et al., 2019). Anthropogenic emissions are assumed aseasonal except for manure management and rice cultivation, for which we apply monthly scaling factors as described by Maasakkers et al. (2016) and Zhang et al. (2018), respectively.

170

Prior monthly emissions for wetlands are given by the high-performance subset of the WetCHARTs ensemble version 1.3.1, which includes the nine ensemble members that best match global GOSAT inversion results (Ma et al., 2021). Lu et al. (2022) found in an inversion of GOSAT data over North America that this high performance subset overestimated wetland methane emissions, particularly at high latitudes. We remove from the ensemble the two members (WetCHARTs models 1923 and 175 2913; Bloom et al., 2017) that are most responsible for this overestimate. Other natural methane emission sources are minor and include open fires, termites, and geological seeps, for which we follow the emissions described in Lu et al. (2022). Methane losses from oxidation and soil uptake are prescribed as in Maasakkers et al. (2019) and are not optimized in the inversion.



180 **Figure 1:** Bottom-up methane emission inventories used as prior estimates for the inversion. Panels show annual mean methane emissions for different sectors. Anthropogenic sectors are given by the gridded versions of the national inventories of Canada (ECCC), the U.S. (EPA GHGI), and Mexico (INECC) reported to the UNFCCC (Maasakkers et al., 2016; Scarpelli et al., 2020, 2022). U.S. oil and gas emissions are updated as described in Sect. 2.2. Wetland emissions are given by the high-performance subset of the WetCHARTs version 1.3.1 wetlands inventory ensemble (Ma et al., 2021), excluding two ensemble members as described in Sect. 2.2. Emissions are shown on the  $0.25^\circ \times 185 0.3125^\circ$  GEOS-Chem grid used for the inversion.

We assume uniform relative error standard deviations for the prior emissions of between 50% and 100% for the different members of our inversion ensemble, with no error covariance between grid cells. Previous inversions that optimized methane emissions over North America assumed prior error standard deviations up to 50%. We inflate errors up to 100% in our ensemble to account for increased errors at high resolution (Maasakkers et al., 2016). Errors for each ensemble member are  
190 chosen as described in Sect. 2.7.

### 2.3 Forward model

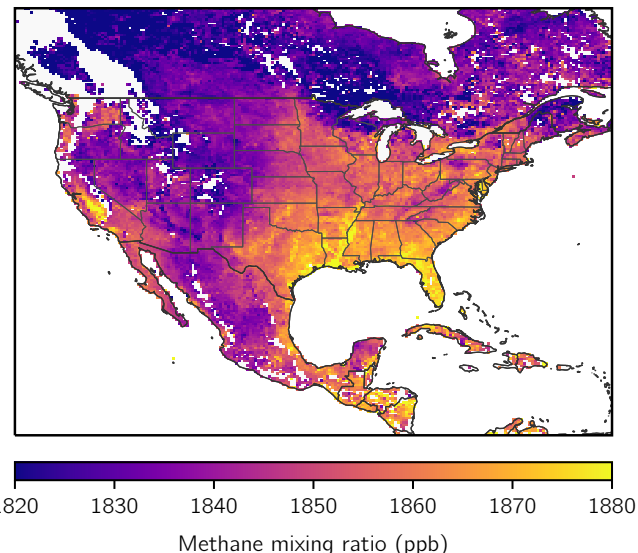
We use the nested version of the GEOS-Chem CTM 12.7.1 (DOI: [10.5281/zenodo.3676008](https://doi.org/10.5281/zenodo.3676008)) at  $0.25^\circ \times 0.3125^\circ$  resolution over North America as the forward model for the inversion. Earlier versions of the methane simulation were described by Wecht et al. (2014a) and Turner et al. (2015). The model is driven by GEOS-FP meteorological fields from the NASA Global  
195 Modeling and Assimilation Office (Lucchesi, 2017). Methane sinks from OH, Cl, soil uptake, and stratospheric oxidation are as described in Maasakkers et al. (2019). Initial conditions for January 1, 2019 and 3-hourly boundary conditions for the year are specified by methane concentration fields from a global GEOS-Chem simulation at  $2^\circ \times 2.5^\circ$  resolution using optimized emissions from a global inversion of TROPOMI observations (Qu et al., 2021).

### 2.4 TROPOMI observations

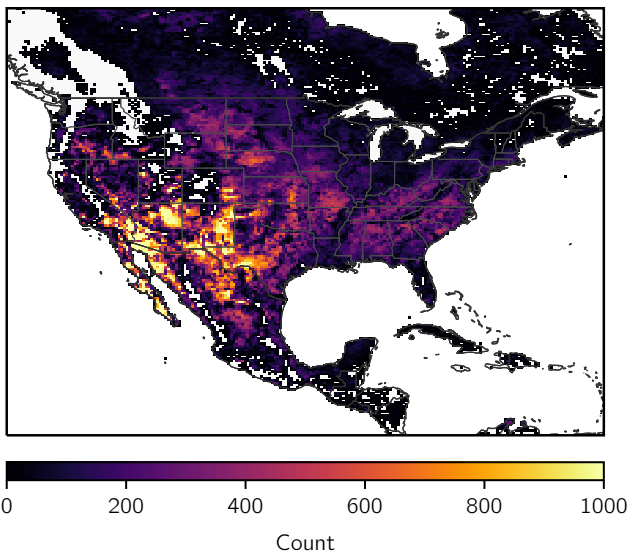
200 TROPOMI has provided daily, global observations of dry column methane mixing ratios at  $7 \text{ km} \times 7 \text{ km}$  nadir pixel resolution since May 2018 and at  $5.5 \text{ km} \times 7 \text{ km}$  nadir pixel resolution since August 2019 (Lorente et al., 2021). TROPOMI measures backscattered solar radiation in the  $2.3 \mu\text{m}$  methane absorption band from a sun-synchronous orbit with a local overpass time of 13:30 (Veefkind et al., 2012). Methane concentrations are inferred from a full-physics retrieval with a  $\sim 3\%$  success rate limited by cloud cover, variable topography, low or heterogeneous albedo, and high aerosol loading (Hasekamp et al., 2019).  
205 We use retrieval v14 as described by Lorente et al. (2021), which has a  $-3.4 \pm 5.6 \text{ ppb}$  bias relative to the Total Carbon Column Observing Network (TCCON). We use only retrievals with quality assessment flag equal to 1.

Previous analyses of TROPOMI data identified surface artifacts (Barré et al., 2021) and spatially variable biases relative to the more accurate but sparser GOSAT data (Jacob et al., 2022). We filter the data to remove snow- and ice-covered scenes using  
210 blended albedo, an empirical parameter developed by Wunch et al. (2011) and suggested for the TROPOMI data by Lorente et al. (2021). We remove scenes with blended albedo greater than 0.75 in non-summer seasons. We also remove scenes with albedo in the shortwave infrared less than 0.05 following de Gouw et al. (2020), which account for most of the remaining unphysical TROPOMI observations (methane mixing ratio less than 1700 ppb), and scenes north of  $50^\circ\text{N}$  in winter.

2019 TROPOMI methane observations



Observational density



215

**Figure 2:** TROPOMI methane observations in 2019. The left panel shows the annual average column dry methane mixing ratios for 2019 averaged on the  $0.25^\circ \times 0.3125^\circ$  GEOS-Chem grid. The right panel shows the number of observations for the year on the same grid. The observations have been filtered as described in Sect. 2.4.

Figure 2 shows the final  $m = 2919358$  observations used for the inversion on the GEOS-Chem  $0.25^\circ \times 0.3125^\circ$  grid. The data  
220 are dense and seasonally consistent across high-emitting regions of CONUS (Fig. S1). The filters preserve 69% of the high-  
quality retrievals of TROPOMI v14 and increase the GOSAT - TROPOMI correlation in all seasons, with the largest increases  
in winter and spring (Fig. S2). Seasonal regional biases decrease by between 7% and 21% and are always within the one  
225 standard deviation range of both the TROPOMI and GOSAT data. Comparison to a GEOS-Chem simulation driven by the  
prior emissions as shown in Fig. S3 shows a mean aseasonal (GEOS-Chem - TROPOMI) bias of  $\xi = 9.1$  ppb over North  
America which we attribute to errors in the boundary conditions. This bias can also be fit as a linear function of degrees latitude  
 $\theta$  as  $\xi = -5.40 + 0.39\theta$ . We correct the bias in our inversion ensemble members by removing either the continental mean  
bias or the latitude-dependent correction from the GEOS-Chem concentrations.

## 2.5 Observing system errors

The observing system error covariance matrix  $\mathbf{S}_0$  includes contributions from forward model, instrument, and representation  
230 errors (Brasseur and Jacob, 2017). Forward model errors include contributions from transport and from random temporal  
variability unresolved by the prior emissions estimate. We calculate the total observing system error variances using the  
residual error method (Heald et al., 2004). This method assumes that the mean difference between the TROPOMI observations  
and the prior GEOS-Chem simulation, calculated here on a seasonal  $2^\circ \times 2^\circ$  grid, is caused by errors in emissions that will be  
corrected by the inversion. The standard deviation of the residual errors after subtracting the mean gridded errors then defines

235 the standard deviation of the observing system errors. We set a minimum error standard deviation of 10 ppb, which applies to 32% of observations. We find a mean observing system error standard deviation of 11.5 ppb, with the largest errors in winter and at high latitudes. The resulting error variances are the diagonal elements of  $\mathbf{S}_0$ . Off-diagonal terms are assumed zero in the absence of better information, which we account for with the regularization factor  $\gamma$  (Chevallier, 2007). We describe the choice of  $\gamma$  in Sect. 2.7.

240 **2.6 Jacobian matrix**

Constructing the Jacobian matrix  $\mathbf{K}$  for our inversion would normally require conducting a 1-year perturbation simulation for each of the  $n = 23691$  grid cells optimized. This is computationally intractable. We construct the Jacobian matrix at substantially decreased computational cost using the reduced-rank method introduced by Nesser et al. (2021), which takes advantage of the heterogeneous information content of the TROPOMI observations. This method updates an initial, low-cost  
245 estimate of the Jacobian matrix by perturbing the patterns that best explain the information content of the observing system, constructing a reduced-rank Jacobian matrix that optimally preserves information content.

We construct the initial, low-cost estimate of the Jacobian matrix  $\mathbf{K}^{(0)}$  using the mass-balance approach described by Nesser et al. (2021). We assume that a perturbation of methane emissions  $\Delta x_j$  in grid cell  $j$  with units  $\text{kg m}^{-2} \text{s}^{-1}$  produces column  
250 mixing ratio enhancements  $\Delta y_i$  over grid cell  $i$  according to

$$\Delta y_i = \alpha_{ij} \frac{M_{\text{air}}}{M_{\text{CH}_4}} \frac{Lg}{Up} \Delta x_j \quad (6)$$

where  $\alpha_{ij} \in [0, 1]$  is a dimensionless coefficient providing a crude representation of turbulent diffusion,  $M_{\text{air}}$  and  $M_{\text{CH}_4}$  are  
255 the molecular weights of dry air and methane, respectively,  $L$  is a ventilation length scale equal to the square root of the grid cell area,  $g$  is gravitational acceleration,  $U$  is the wind speed taken here as  $5 \text{ km h}^{-1}$ , and  $p$  is the surface pressure taken here as 1000 hPa. The use of  $\alpha_{ij}$  produces off-diagonal structure in  $\mathbf{K}^{(0)}$ , which we found in Nesser et al. (2021) to be necessary for an effective first estimate. We apply a simple isotropic turbulent diffusion scheme in which the influence of emissions spreads linearly to concentric rings of grid cells. This is represented as  $\alpha_{ij} = (8 - \|i - j\|)/36c$ , where  $\|i - j\| = \{0, 1, \dots, 7\}$  gives  
260 the distance in latitude or longitude grid cell index between  $i$  and  $j$ , 36 is the sum of  $\|i - j + 1\|$  values, and  $c$  gives the number of grid cells in the corresponding concentric ring. For  $\|i - j\| \geq 8$ ,  $\alpha_{ij} = 0$ .

We use  $\mathbf{K}^{(0)}$  together with the error covariance matrices  $\mathbf{S}_A$  and  $\mathbf{S}_0$  to calculate the initial patterns of information content that are perturbed in the forward model. We calculate the prior pre-conditioned Hessian (Eq. (2)) using  $\mathbf{K}^{(0)}$  and perform its  
265 eigendecomposition. The resulting matrix of eigenvectors  $\mathbf{V}^{(0)}$  is related to the patterns of information content via  $\mathbf{S}_A^{1/2} \mathbf{V}^{(0)}$ ,

which is equivalent to the eigenvector matrix of the averaging kernel matrix calculated with  $\mathbf{K}^{(0)}$  (Bousserez and Henze, 2018). We perturb the  $k_1 = 434$  eigenvectors that capture 50% of the DOFS generated with  $\mathbf{K}^{(0)}$ . We then apply an optimal operator that restores the original state dimension and minimizes information content loss to yield an updated reduced-rank Jacobian matrix estimate  $\mathbf{K}^{(1)}$ . We recompute the eigenvectors, perturb the  $k_2 = 1952$  eigenvectors that explain 80% of the initial DOFS, and construct the final reduced-rank Jacobian matrix  $\mathbf{K}^{(2)}$ . This iterative update scheme optimizes the information content of the posterior solution while reducing the computational cost by an order of magnitude (Nesser et al., 270 2021).

## 2.7 Inversion ensemble

The posterior error covariance matrix that results from Bayesian optimization (Eq. (4)) does not account for errors in inversion parameters including the prior and observing system error covariance matrices (Houweling et al., 2014). The analytical solution readily allows for the creation of an ensemble of inversions that reflects the sensitivity of the results to the chosen setup including parameters. Table 1 summarizes our quality-controlled ensemble of inversions. We conduct inversions that do or do not optimize the boundary conditions and apply either a latitudinal or mean bias correction to the prior (model - observation) difference as driven by boundary condition biases. For each inversion, we choose the relative prior error (50%, 275 280 285 290 295 300 305 310 315 320 325 330 335 340 345 350 355 360 365 370 375 380 385 390 395 400 405 410 415 420 425 430 435 440 445 450 455 460 465 470 475 480 485 490 495 500 505 510 515 520 525 530 535 540 545 550 555 560 565 570 575 580 585 590 595 600 605 610 615 620 625 630 635 640 645 650 655 660 665 670 675 680 685 690 695 700 705 710 715 720 725 730 735 740 745 750 755 760 765 770 775 780 785 790 795 800 805 810 815 820 825 830 835 840 845 850 855 860 865 870 875 880 885 890 895 900 905 910 915 920 925 930 935 940 945 950 955 960 965 970 975 980 985 990 995 1000 1005 1010 1015 1020 1025 1030 1035 1040 1045 1050 1055 1060 1065 1070 1075 1080 1085 1090 1095 1100 1105 1110 1115 1120 1125 1130 1135 1140 1145 1150 1155 1160 1165 1170 1175 1180 1185 1190 1195 1200 1205 1210 1215 1220 1225 1230 1235 1240 1245 1250 1255 1260 1265 1270 1275 1280 1285 1290 1295 1300 1305 1310 1315 1320 1325 1330 1335 1340 1345 1350 1355 1360 1365 1370 1375 1380 1385 1390 1395 1400 1405 1410 1415 1420 1425 1430 1435 1440 1445 1450 1455 1460 1465 1470 1475 1480 1485 1490 1495 1500 1505 1510 1515 1520 1525 1530 1535 1540 1545 1550 1555 1560 1565 1570 1575 1580 1585 1590 1595 1600 1605 1610 1615 1620 1625 1630 1635 1640 1645 1650 1655 1660 1665 1670 1675 1680 1685 1690 1695 1700 1705 1710 1715 1720 1725 1730 1735 1740 1745 1750 1755 1760 1765 1770 1775 1780 1785 1790 1795 1800 1805 1810 1815 1820 1825 1830 1835 1840 1845 1850 1855 1860 1865 1870 1875 1880 1885 1890 1895 1900 1905 1910 1915 1920 1925 1930 1935 1940 1945 1950 1955 1960 1965 1970 1975 1980 1985 1990 1995 2000 2005 2010 2015 2020 2025 2030 2035 2040 2045 2050 2055 2060 2065 2070 2075 2080 2085 2090 2095 2100 2105 2110 2115 2120 2125 2130 2135 2140 2145 2150 2155 2160 2165 2170 2175 2180 2185 2190 2195 2200 2205 2210 2215 2220 2225 2230 2235 2240 2245 2250 2255 2260 2265 2270 2275 2280 2285 2290 2295 2300 2305 2310 2315 2320 2325 2330 2335 2340 2345 2350 2355 2360 2365 2370 2375 2380 2385 2390 2395 2400 2405 2410 2415 2420 2425 2430 2435 2440 2445 2450 2455 2460 2465 2470 2475 2480 2485 2490 2495 2500 2505 2510 2515 2520 2525 2530 2535 2540 2545 2550 2555 2560 2565 2570 2575 2580 2585 2590 2595 2600 2605 2610 2615 2620 2625 2630 2635 2640 2645 2650 2655 2660 2665 2670 2675 2680 2685 2690 2695 2700 2705 2710 2715 2720 2725 2730 2735 2740 2745 2750 2755 2760 2765 2770 2775 2780 2785 2790 2795 2800 2805 2810 2815 2820 2825 2830 2835 2840 2845 2850 2855 2860 2865 2870 2875 2880 2885 2890 2895 2900 2905 2910 2915 2920 2925 2930 2935 2940 2945 2950 2955 2960 2965 2970 2975 2980 2985 2990 2995 3000 3005 3010 3015 3020 3025 3030 3035 3040 3045 3050 3055 3060 3065 3070 3075 3080 3085 3090 3095 3100 3105 3110 3115 3120 3125 3130 3135 3140 3145 3150 3155 3160 3165 3170 3175 3180 3185 3190 3195 3200 3205 3210 3215 3220 3225 3230 3235 3240 3245 3250 3255 3260 3265 3270 3275 3280 3285 3290 3295 3300 3305 3310 3315 3320 3325 3330 3335 3340 3345 3350 3355 3360 3365 3370 3375 3380 3385 3390 3395 3400 3405 3410 3415 3420 3425 3430 3435 3440 3445 3450 3455 3460 3465 3470 3475 3480 3485 3490 3495 3500 3505 3510 3515 3520 3525 3530 3535 3540 3545 3550 3555 3560 3565 3570 3575 3580 3585 3590 3595 3600 3605 3610 3615 3620 3625 3630 3635 3640 3645 3650 3655 3660 3665 3670 3675 3680 3685 3690 3695 3700 3705 3710 3715 3720 3725 3730 3735 3740 3745 3750 3755 3760 3765 3770 3775 3780 3785 3790 3795 3800 3805 3810 3815 3820 3825 3830 3835 3840 3845 3850 3855 3860 3865 3870 3875 3880 3885 3890 3895 3900 3905 3910 3915 3920 3925 3930 3935 3940 3945 3950 3955 3960 3965 3970 3975 3980 3985 3990 3995 4000 4005 4010 4015 4020 4025 4030 4035 4040 4045 4050 4055 4060 4065 4070 4075 4080 4085 4090 4095 4100 4105 4110 4115 4120 4125 4130 4135 4140 4145 4150 4155 4160 4165 4170 4175 4180 4185 4190 4195 4200 4205 4210 4215 4220 4225 4230 4235 4240 4245 4250 4255 4260 4265 4270 4275 4280 4285 4290 4295 4300 4305 4310 4315 4320 4325 4330 4335 4340 4345 4350 4355 4360 4365 4370 4375 4380 4385 4390 4395 4400 4405 4410 4415 4420 4425 4430 4435 4440 4445 4450 4455 4460 4465 4470 4475 4480 4485 4490 4495 4500 4505 4510 4515 4520 4525 4530 4535 4540 4545 4550 4555 4560 4565 4570 4575 4580 4585 4590 4595 4600 4605 4610 4615 4620 4625 4630 4635 4640 4645 4650 4655 4660 4665 4670 4675 4680 4685 4690 4695 4700 4705 4710 4715 4720 4725 4730 4735 4740 4745 4750 4755 4760 4765 4770 4775 4780 4785 4790 4795 4800 4805 4810 4815 4820 4825 4830 4835 4840 4845 4850 4855 4860 4865 4870 4875 4880 4885 4890 4895 4900 4905 4910 4915 4920 4925 4930 4935 4940 4945 4950 4955 4960 4965 4970 4975 4980 4985 4990 4995 5000 5005 5010 5015 5020 5025 5030 5035 5040 5045 5050 5055 5060 5065 5070 5075 5080 5085 5090 5095 5100 5105 5110 5115 5120 5125 5130 5135 5140 5145 5150 5155 5160 5165 5170 5175 5180 5185 5190 5195 5200 5205 5210 5215 5220 5225 5230 5235 5240 5245 5250 5255 5260 5265 5270 5275 5280 5285 5290 5295 5300 5305 5310 5315 5320 5325 5330 5335 5340 5345 5350 5355 5360 5365 5370 5375 5380 5385 5390 5395 5400 5405 5410 5415 5420 5425 5430 5435 5440 5445 5450 5455 5460 5465 5470 5475 5480 5485 5490 5495 5500 5505 5510 5515 5520 5525 5530 5535 5540 5545 5550 5555 5560 5565 5570 5575 5580 5585 5590 5595 5600 5605 5610 5615 5620 5625 5630 5635 5640 5645 5650 5655 5660 5665 5670 5675 5680 5685 5690 5695 5700 5705 5710 5715 5720 5725 5730 5735 5740 5745 5750 5755 5760 5765 5770 5775 5780 5785 5790 5795 5800 5805 5810 5815 5820 5825 5830 5835 5840 5845 5850 5855 5860 5865 5870 5875 5880 5885 5890 5895 5900 5905 5910 5915 5920 5925 5930 5935 5940 5945 5950 5955 5960 5965 5970 5975 5980 5985 5990 5995 6000 6005 6010 6015 6020 6025 6030 6035 6040 6045 6050 6055 6060 6065 6070 6075 6080 6085 6090 6095 6100 6105 6110 6115 6120 6125 6130 6135 6140 6145 6150 6155 6160 6165 6170 6175 6180 6185 6190 6195 6200 6205 6210 6215 6220 6225 6230 6235 6240 6245 6250 6255 6260 6265 6270 6275 6280 6285 6290 6295 6300 6305 6310 6315 6320 6325 6330 6335 6340 6345 6350 6355 6360 6365 6370 6375 6380 6385 6390 6395 6400 6405 6410 6415 6420 6425 6430 6435 6440 6445 6450 6455 6460 6465 6470 6475 6480 6485 6490 6495 6500 6505 6510 6515 6520 6525 6530 6535 6540 6545 6550 6555 6560 6565 6570 6575 6580 6585 6590 6595 6600 6605 6610 6615 6620 6625 6630 6635 6640 6645 6650 6655 6660 6665 6670 6675 6680 6685 6690 6695 6700 6705 6710 6715 6720 6725 6730 6735 6740 6745 6750 6755 6760 6765 6770 6775 6780 6785 6790 6795 6800 6805 6810 6815 6820 6825 6830 6835 6840 6845 6850 6855 6860 6865 6870 6875 6880 6885 6890 6895 6900 6905 6910 6915 6920 6925 6930 6935 6940 6945 6950 6955 6960 6965 6970 6975 6980 6985 6990 6995 7000 7005 7010 7015 7020 7025 7030 7035 7040 7045 7050 7055 7060 7065 7070 7075 7080 7085 7090 7095 7100 7105 7110 7115 7120 7125 7130 7135 7140 7145 7150 7155 7160 7165 7170 7175 7180 7185 7190 7195 7200 7205 7210 7215 7220 7225 7230 7235 7240 7245 7250 7255 7260 7265 7270 7275 7280 7285 7290 7295 7300 7305 7310 7315 7320 7325 7330 7335 7340 7345 7350 7355 7360 7365 7370 7375 7380 7385 7390 7395 7400 7405 7410 7415 7420 7425 7430 7435 7440 7445 7450 7455 7460 7465 7470 7475 7480 7485 7490 7495 7500 7505 7510 7515 7520 7525 7530 7535 7540 7545 7550 7555 7560 7565 7570 7575 7580 7585 7590 7595 7600 7605 7610 7615 7620 7625 7630 7635 7640 7645 7650 7655 7660 7665 7670 7675 7680 7685 7690 7695 7700 7705 7710 7715 7720 7725 7730 7735 7740 7745 7750 7755 7760 7765 7770 7775 7780 7785 7790 7795 7800 7805 7810 7815 7820 7825 7830 7835 7840 7845 7850 7855 7860 7865 7870 7875 7880 7885 7890 7895 7900 7905 7910 7915 7920 7925 7930 7935 7940 7945 7950 7955 7960 7965 7970 7975 7980 7985 7990 7995 8000 8005 8010 8015 8020 8025 8030 8035 8040 8045 8050 8055 8060 8065 8070 8075 8080 8085 8090 8095 8100 8105 8110 8115 8120 8125 8130 8135 8140 8145 8150 8155 8160 8165 8170 8175 8180 8185 8190 8195 8200 8205 8210 8215 8220 8225 8230 8235 8240 8245 8250 8255 8260 8265 8270 8275 8280 8285 8290 8295 8300 8305 8310 8315 8320 8325 8330 8335 8340 8345 8350 8355 8360 8365 8370 8375 8380 8385 8390 8395 8400 8405 8410 8415 8420 8425 8430 8435 8440 8445 8450 8455 8460 8465 8470 8475 8480 8485 8490 8495 8500 8505 8510 8515 8520 8525 8530 8535 8540 8545 8550 8555 8560 8565 8570 8575 8580 8585 8590 8595 8600 8605 8610 8615 8620 8625 8630 8635 8640 8645 8650 8655 8660 8665 8670 8675 8680 8685 8690 8695 8700 8705 8710 8715 8720 8725 8730 8735 8740 8745 8750 8755 8760 8765 8770 8775 8780 8785 8790 8795 8800 8805 8810 8815 8820 8825 8830 8835 8840 8845 8850 8855 8860 8865 8870 8875 8880 8885 8890 8895 8900 8905 8910 8915 8920 8925 8930 8935 8940 8945 8950 8955 8960 8965 8970 8975 8980 8985 8990 8995 9000 9005 9010 9015 9020 9025 9030 9035 9040 9045 9050 9055 9060 9065 9070 9075 9080 9085 9090 9095 9100 9105 9110 9115 9120 9125 9130 9135 9140 9145 9150 9155 9160 9165 9170 9175 9180 9185 9190 9195 9200 9205 9210 9215 9220 9225 9230 9235 9240 9245 9250 9255 9260 9265 9270 9275 9280 9285 9290 9295 9300 9305 9310 9315 9320 9325 9330 9335 9340 9345 9350 9355 9360 9365 9370 9375 9380 9385 9390 9395 9400 9405 9410 9415 9420 9425 9430 9435 9440 9445 9450 9455 9460 9465 9470 9475 9480 9485 9490 9495 9500 9505 9510 9515 9520 9525 9530 9535 9540 9545 9550 9555 9560 9565 9570 9575 9580 9585 9590 9595 9600 9605 9610 9615 9620 9625 9630 9635 9640 9645 9650 9655 9660 9665 9670 9675 9680 9685 9690 9695 9700 9705 9710 9715 9720 9725 9730 9735 9740 9745 9750 9755 9760 9765 9770 9775 9780 9785 9790 9795 9800 9805 9810 9815 9820 9825 9830 9835 9840 9845 9850 9855 9860 9865 9870 9875 9880 9885 9890 9895 9900 9905 9910 9915 9920 9925 9930 9935 9940 9945 9950 9955 9960 9965 9970 9975 9980 9985 9990 9995 9999 10000 10005 10010 10015 10020 10025 10030 10035 10040 10045 10050 10055 10060 10065 10070 10075 10080 10085 10090 10095 10100 10105 10110 10115 10120 10125 10130 10135 10140 10145 10150 10155 10160 10165 10170 10175 10180 10185 10190 10195 10200 10205 10210 10215 10220 10225 10230 10235 10240 10245 10250 10255 10260 10265 10270 10275 10280 10285 10290 10295 10300 10305 10310 10315 10320 10325 10330 10335 10340 10345 10350 10355 10360 10365 10370 10375 10380 10385 10390 10395 10400 10405 10410 10415 10420 10425 10430 10435 10440 10445 10450 10455 10460 10465 10470 10475 10480 10485 10490 10495 10500 10505 10510 10515 10520 10525 10530 10535 10540 10545 10550 10555 10560 10565 10570 10575 10580 10585 10590 10595 10600 10605 10610 10615 10620 10625 10630 10635 10640 10645 10650 10655 10660 10665 10670 10675 10680 10685 10690 10695 10700 10705 10710 10715 10720 10725 10730 10735 10740 10745 10750 10755 10760 10765 10770 10775 10780 10785 10790 10795 10800 10805 10810 10815 10820 10825 10830 10835 10840 10845 10850 10855 10860 10865 10870 10875 10880 10885 10890 10895 10900 10905 10910 10915 10920 10925 10930 10935 10940 10945 10950 10955 10960 10965 10970 10975 10980 10985 10990 10995 11000 11005 11010 11015 11020 11025 11030 11035 11040 11045 11050 11055 11060 11065 11070 11075 11080 11085 11090 11095 11100 11105 11110 11115 11120 11125 11130 11135 11140 11145 11150 11155 11160 11165 11170 11175 11180 11185 11190 11195 11200 11205 11210 11215 11220 11225 11230 11235 11240 11245 11250 11255 11260 11265 11270 11275 11280 11285 11290 11295 11300 11305 11310 11315 11320 11325 11330 11335 11340 11345 11350 11355 11360 11365 11370 11375 11380 11385 11390 11395 11400 11405 11410 11415 11420 11425 11430 11435 11440 11445 11450 11455 11460 11465 11470 11475 11480 11485 11490 11495 11500 11505 11510 11515 11520 11525 11530 11535 11540 11545 11550 11555 11560 11565 11570 11575 11580 11585 11590 11595 11600 11605 11610 11615 11620 11625 11630 11635 11640

75%, or 100%) and regularization factor (between 0.175 and 0.5) so that the prior term of the cost function evaluated at the posterior solution  $J_A(\hat{\mathbf{x}}) = (\hat{\mathbf{x}} - \mathbf{x}_A)^T \mathbf{S}_A^{-1} (\hat{\mathbf{x}} - \mathbf{x}_A)$  averages to 1 across all grid cells optimized by the reduced-rank inversion as expected from the chi-square distribution, which  $J_A(\mathbf{x})$  definitionally follows (Lu et al., 2021). This yields an ensemble of 295 eight quality-controlled inversions with indistinguishable validity. All inversions have few grid cells with negative emissions, most of which are on the same order of magnitude as the soil sink. Unless otherwise noted, our results give the mean posterior emissions for the ensemble, with uncertainty ranges given by the ensemble range.

## 2.8 Source attribution

The high resolution of the inversion facilitates the attribution of the posterior emission estimates to individual source sectors 300 or regions, including states and urban areas. We aggregate the native resolution emission and error estimates to the corresponding  $p$  sectors, states, or urban areas using a summation matrix  $\mathbf{W} \in \mathbb{R}^{p \times n}$ . The rows of  $\mathbf{W}$  are given by the relative contribution of each grid cell to each source category. For sectoral attribution, the rows are given by the relative, area-normalized contribution of each grid cell to a given sector in the prior emission estimate. For state attribution, the rows are given by the fraction of each grid cell within a given state. For urban area attribution, the rows have binary values depending 305 on whether the grid cell overlaps with a given urban area. If the grid cell contains multiple urban areas, the fractional contribution of the grid cell to a given urban area is used instead. The reduced-dimension posterior estimate  $\hat{\mathbf{x}}_{\text{FR,red}}$ , posterior covariance matrix  $\hat{\mathbf{S}}_{\mathbf{K},\text{red}}$ , and averaging kernel matrix  $\mathbf{A}_{\mathbf{K},\text{red}}$  are then given by

$$\hat{\mathbf{x}}_{\text{FR,red}} = \mathbf{W}\hat{\mathbf{x}}_{\text{FR}}, \quad (7)$$

$$\hat{\mathbf{S}}_{\mathbf{K},\text{red}} = \mathbf{W}\hat{\mathbf{S}}_{\mathbf{K}}\mathbf{W}^T, \text{ and} \quad (8)$$

$$\mathbf{A}_{\mathbf{K},\text{red}} = \mathbf{W}\mathbf{A}_{\mathbf{K}}\mathbf{W}^*, \quad (9)$$

310

where  $\mathbf{W}^* = \mathbf{W}^T(\mathbf{W}\mathbf{W}^T)^{-1}$  is the Moore-Penrose pseudo inverse (Calisesi et al., 2005). In the case of disaggregating our emission estimates to individual landfills, we scale the posterior estimate in the corresponding grid cell by the fraction of emissions attributed to landfills in the prior estimate. These approaches to source aggregation and disaggregation assume that the prior fractional sectoral contributions are correct in each grid cell and that emission sources are evenly distributed in grid 315 cells that cross state lines. The uncertainty of this method is not reflected in the reported error bounds, but the high resolution of our emission estimates decreases the influence of these assumptions relative to coarser resolution estimates. Newly developed methods use prior and posterior error covariances to improve upon these assumptions (Cusworth et al., 2021).

## 3 Results and discussion

Figure 3 shows the ensemble mean posterior scale factors relative to the annual average prior emission estimate as described 320 in Sect. 2.2 (left) and the corresponding averaging kernel sensitivities (right). Grid cells unoptimized by the inversion (mean

averaging kernel sensitivity less than 0.05) are left blank. We find 772 (421 - 1279) DOFS for the domain, where the values in parentheses here and elsewhere are the quality-controlled, eight-member inversion ensemble minimum and maximum, respectively. This represents a large increase in information content relative to past inversions over North America: Lu et al. (2022) found 114 DOFS in a joint inversion of data from GOSAT and the National Oceanic and Atmospheric Administration's (NOAA) GLOBALVIEWplus ObsPack in situ data, while Shen et al. (2022) found 201 DOFS in an inversion of TROPOMI observations over 14 oil and gas basins. This increase reflects both the improved coverage from TROPOMI and the benefit of achieving  $0.25^\circ \times 0.3125^\circ$  resolution on the continental scale. Of these DOFS, 641 (350 – 1058) are found for CONUS, 86 (53 – 134) for Mexico, and 37 (15 - 69) for Canada. The high information content for CONUS reflects both the large emissions (Fig. 1) and the high density and consistency of TROPOMI observations (Fig. 2). As a result, we focus our discussion on CONUS. We isolate anthropogenic emissions by removing contributions from wetlands and other natural sources following Sect. 2.8. We compare our posterior emissions to the 2023 EPA GHGI inventory for 2019, including to the emission estimates for individual states (EPA, 2023a, b). We remove emissions from Hawaii and Alaska from the GHGI total using these state estimates, which account for less than 0.5% of the national total.

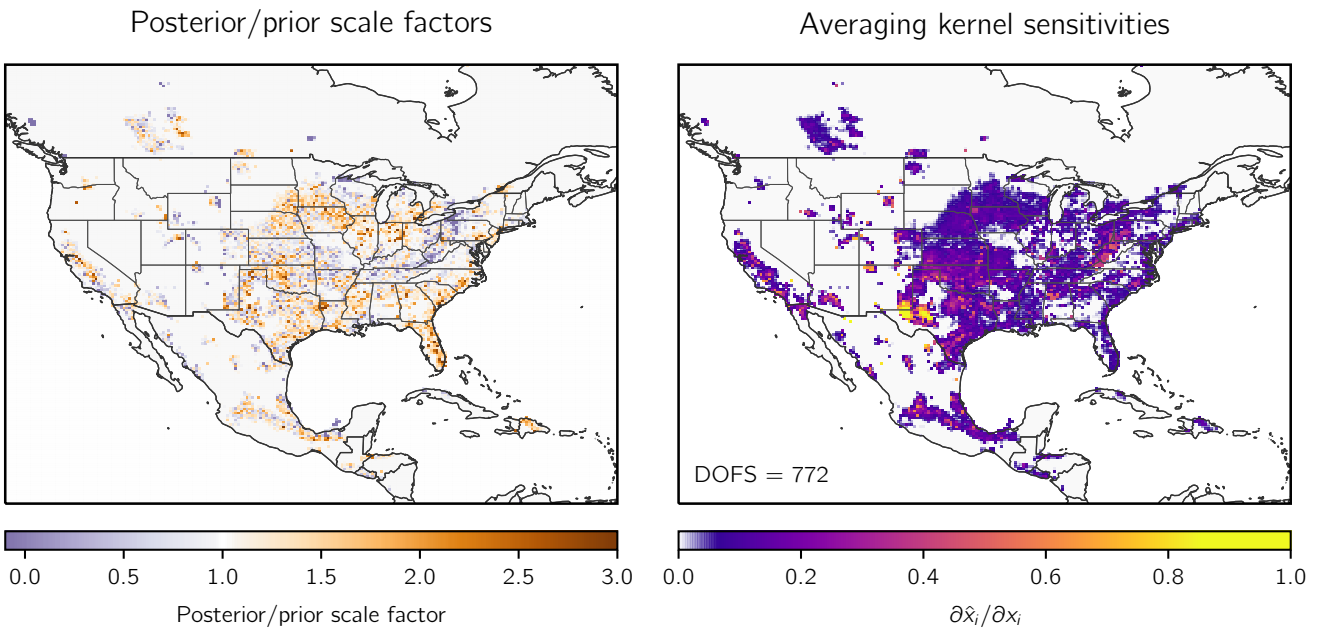


**Figure 3:** Optimization of methane emissions for 2019 by inversion of TROPOMI observations. The left panel shows the scale factors relative to the prior estimate for the inversion given by gridded versions of the national anthropogenic emissions inventories for the U.S. (EPA GHGI), Mexico (INECC), and Canada (ECCC), with U.S. oil and gas emissions updated as described in Sect. 2.2, and by WetCHARTs wetland emissions (top left panel of Fig. 1). The right panel shows the observing system information content as measured by the averaging kernel sensitivities (the diagonal elements of the averaging kernel matrix). Values of 1 indicate that TROPOMI quantifies emissions independently of the prior estimate, while values of 0 indicate that emissions are not optimized by the inversion. The sum of the averaging kernel sensitivities gives the degrees of freedom for signal (DOFS), shown inset, which defines the number of independent pieces of information quantified by the observing system. Grid cells with averaging kernel sensitivities less than 0.05 are left blank.

345 We evaluate the inversion results by comparing simulated observations from GEOS-Chem driven by either the prior or the mean posterior emissions to TROPOMI observations and to independent in situ surface and tower observations from NOAA's GLOBALVIEWplus CH<sub>4</sub> ObsPack v3.0 database (Cooperative Global Atmospheric Data Integration Project, 2019). We follow Lu et al. (2021) and use only daytime ObsPack observations with outliers excluded. We use monthly average ObsPack observations over CONUS to increase consistency with the annual temporal resolution of our inversion and its distribution of  
350 information content. Compared to TROPOMI, both the prior and posterior GEOS-Chem simulations produce similar coefficients of determination ( $R^2$ ) and root mean squared errors (RMSEs). Compared to ObsPack, the posterior simulation improves upon the prior simulation, increasing  $R^2$  from 0.55 to 0.65 and decreasing the RMSE from 80 ppb to 73 ppb, similar to previous inversions of satellite data (Lu et al., 2021). The broad agreement of both simulations with observations reflects the high quality of the prior emission estimate in North America (Maasakkers et al., 2019).

355

We also compare the TROPOMI v14 data used here to the most recent data (v19), which has improved bias corrections and performance compared to GOSAT in North America (Balasus et al., 2023). We define the grid cells containing observations sensitive to the optimized emissions by calculating the row-wise sum of the Jacobian matrix weighted by the prior and observing system error standard deviations, limited to emission grid cells with averaging kernel sensitivities greater than 0.05.  
360 Of the 95% of observation grid cells most sensitive to the optimized emissions, only 14% have an average mean-bias corrected ( $v14 - v19$ ) difference greater than 5 ppb and less than 2% have a difference greater than 10 ppb. We similarly define the observation grid cells that influence the optimized emission grid cells using the Jacobian matrix columns. We find that the average mean-bias corrected ( $v14 - v19$ ) difference for the observational grid cells influenced by optimized grid cells is -0.05 ppb with a standard deviation of 0.1 ppb, indicating that there is little bias in the observations that influence any single grid  
365 cell. We finally find no correlation ( $R^2 = 0.03$ ) between our posterior scaling factors and the mean ( $v14 - v19$ ) difference, suggesting that biases in the v14 data do not influence our posterior emissions.

### 3.1 CONUS sectoral emissions

We find posterior anthropogenic methane emissions of 30.9 (30.0 - 31.8) Tg a<sup>-1</sup> for CONUS in 2019, a 13% increase from the GHGI estimate of 27.3 (25.1 - 30.6) Tg a<sup>-1</sup>, where the values in parentheses represent the GHGI 95% confidence interval (EPA,  
370 2023a). This estimate excludes Alaska and Hawaii, which likely represent a small (~1%) contribution to the national anthropogenic total (Miller et al., 2016; Konan and Chan, 2010). Lu et al. (2022) found larger anthropogenic emissions of 36.2 (32.1 - 37.6) Tg a<sup>-1</sup> over the same domain for 2017 by optimizing emissions and trends in a joint inversion of GOSAT and in situ observations for 2010 to 2017. Worden et al. (2022) found lower anthropogenic emissions of 27.6 (24.3 – 30.9) Tg a<sup>-1</sup> over the U.S. for 2019 by regridding global inversions of GOSAT data that optimized emissions at 2° × 2.5° resolution using  
375 uncertainties for the prior and posterior estimates. Deng et al. (2022) reviewed an ensemble of global inversions and

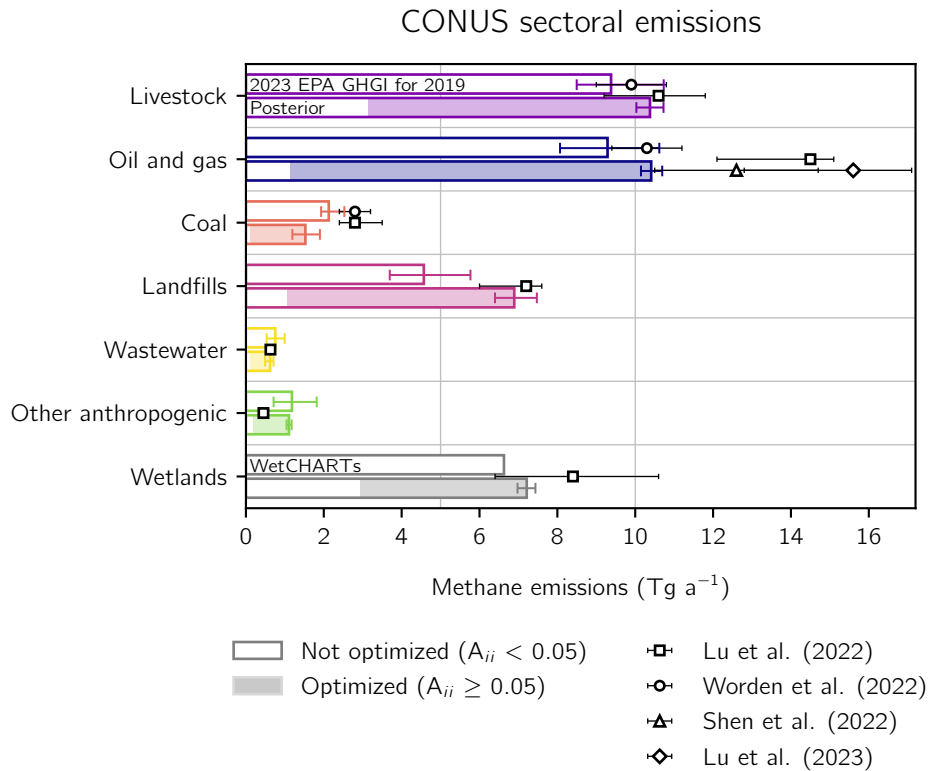


**Figure 4:** Sectoral methane emissions in the contiguous United States (CONUS) for 2019. The 2023 EPA GHGI emissions for 2019 (top bars) and posterior estimates given by inversion of TROPOMI data for 2019 (bottom bars) are shown for different sectors. For wetland emissions we show the WetCHARTs estimate (top bar). The shading corresponds to emissions in grid cells that are optimized by the inversion (grid cells with averaging kernel sensitivities greater than 0.05), while the white represents emissions not optimized by the inversion so that the posterior defaults to the prior estimate. Error bars on the GHGI emissions represent the GHGI 95% confidence intervals. Error bars on the posterior emissions are given by the spread of the eight-member inversion ensemble. Also shown are independent sectoral emission estimates from previous inversions.

380

found median U.S. posterior anthropogenic emissions for 2019 of 26.5 (20.8 - 38.7) Tg a<sup>-1</sup> with GOSAT data and 31.9 (23.9 - 43.1) Tg a<sup>-1</sup> with in situ data.

385

We allocate our national total to individual emission sectors using the attribution method described in Sect. 2.8. From the off-diagonal structure of  $\hat{\mathbf{S}}_{K,\text{red}}$  (Eq. (8)), we find very low posterior error correlation between all anthropogenic and biogenic

390

sectors (mean error correlation coefficients less than 0.2), indicating that we can accurately separate sectoral emissions. Figure 4 and Table 2 summarize the results compared to the GHGI. Livestock, oil and gas, and landfills account for 89% of posterior anthropogenic emissions and all increase relative to the GHGI. We find a significant decrease from the GHGI only for coal. For these four sectors, we find sectoral averaging kernel sensitivities between 0.47 and 0.91, larger than the values found by Lu et al. (2022) from GOSAT and in situ data, indicating that TROPOMI constrains most of the emissions from these sources.

395

We find a small but significant increase in wetland emissions that is consistent with the large range found by Lu et al.

**Table 2:** 2019 methane emissions for the contiguous United States (CONUS).

	Inventory emissions <sup>1</sup>	Posterior emissions <sup>2</sup>	Sensitivity <sup>3</sup>
<b>Total sources (Tg a<sup>-1</sup>)</b>	35.1	39.3 (38.2 - 40.3)	
<b>Anthropogenic sources</b>	27.3 (25.1 - 30.6)	30.9 (30.0 - 31.8)	
Livestock	9.4 (8.5 - 10.7)	10.4 (10.0 - 10.7)	0.66 (0.55 - 0.76)
Oil and natural gas	9.3 (8.1 - 10.6)	10.4 (10.1 - 10.7)	0.91 (0.88 - 0.95)
Coal	2.1 (1.9 - 2.5)	1.5 (1.2 - 1.9)	0.60 (0.45 - 0.80)
Landfills	4.6 (3.7 - 5.8)	6.9 (6.4 - 7.5)	0.47 (0.34 - 0.64)
Wastewater	0.8 (0.5 - 1.0)	0.6 (0.5 - 0.7)	0.33 (0.16 - 0.60)
Other anthropogenic	1.2 (0.7 - 1.8)	1.1 (1.0 - 1.2)	0.59 (0.44 - 0.76)
<b>Natural sources</b>	7.8	8.4 (8.1 - 8.6)	
Wetlands	6.6	7.2 (7.0 - 7.4)	0.35 (0.16 - 0.55)
Other biogenic	1.1	1.2 (1.2 - 1.2)	0.25 (0.19 - 0.32)

<sup>1</sup>Inventory estimates of sectoral methane emissions. Anthropogenic emissions are given by the EPA 2023 GHGI for 2019, with error ranges inferred from the sum in quadrature of bottom-up subsector errors given as 95% confidence intervals. Wetland emissions are from a subset of the high performance WetCHARTs ensemble version 1.3.1; see Sect. 2.2 for details.

400 <sup>2</sup>Optimized emissions from the inversion of TROPOMI data, with the range from the eight members of the inversion ensemble shown in parentheses.

<sup>3</sup>The sensitivity of the posterior emissions to the observing system as given by the diagonal elements of the sectoral averaging kernel matrix calculated as described in Sect. 2.8. The values in parentheses give the range of the inversion ensemble. Values range from 0 (no sensitivity) to 1 (full sensitivity).

405

(2022). However, the reduced-rank observing system only optimizes about half of wetland emissions, with most of the inferred increase limited to the south eastern coast, including South Carolina, Georgia, and eastern Florida.

410

Landfill emissions show the largest relative and absolute increase from the GHGI for 2019. We find posterior emissions of 6.9 (6.4 - 7.5) Tg a<sup>-1</sup>, a 51% increase relative to the GHGI estimate of 4.6 (3.7 - 5.8) Tg a<sup>-1</sup>. Lu et al. (2022) found similar posterior landfill emissions of 7.5 (5.9 - 7.7) Tg a<sup>-1</sup> for 2017. We attribute the GHGI underestimate to two components of the GHGRP landfill inventory methodologies that produce key inputs for the GHGI, which we discuss in detail in Sect. 3.2. First, for landfills with gas recovery systems, the GHGRP assumes too-high collection efficiencies. Second, the GHGRP does not account for site-specific operations that may produce anomalous emissions.

415

Coal mining emissions of 1.5 (1.2 - 1.9) Tg a<sup>-1</sup> exhibit the largest decrease in sectoral emissions relative to the GHGI estimate of 2.1 (1.9 - 2.5) Tg a<sup>-1</sup>. Lu et al. (2022) found much larger posterior emissions of 2.9 (2.3 - 3.4) Tg a<sup>-1</sup> for 2017, and Worden et al. (2022) found similar values of  $2.8 \pm 0.4$  Tg a<sup>-1</sup> for 2019. Compared to these studies, we achieve a stronger constraint on coal emissions as measured by averaging kernel sensitivities, reflecting the increased coverage from TROPOMI compared to GOSAT. Our lower estimate better reflects the 30% decrease in CONUS coal production from 2012 to 2019 (EIA, 2021),

which is also shown in the 30% decrease in GHGI coal emissions over the same period (EPA, 2023a). As expected, emissions correlate with underground coal mining: Appalachia generated 56% of U.S. coal from underground mines in 2019 and 64% of posterior emissions from coal, while the Illinois Basin yielded 30% of U.S. underground coal and 20% of posterior emissions (EIA, 2021).

425

Livestock emissions show broad agreement with the GHGI, with posterior emissions of 10.4 (10.0 - 10.7) Tg a<sup>-1</sup> representing an 11% increase from the GHGI estimate of 9.4 (8.5 - 10.7) Tg a<sup>-1</sup>. Lu et al. (2022) found similar mean posterior livestock emissions of 10.4 (8.8 - 11.6) Tg a<sup>-1</sup> over CONUS for 2017, and Worden et al. (2022) found similar values of  $9.9 \pm 0.4$  Tg a<sup>-1</sup> for 2019. Yu et al. (2021) conducted a seasonal inversion of aircraft observations over the North Central U.S. and South Central Canada for 2017 to 2018 and found mean posterior livestock emissions of 5.5 (5.1 - 6.2) Tg a<sup>-1</sup>, which agrees with our livestock estimate of 5.4 (5.2 - 5.6) Tg a<sup>-1</sup> over the same region. Despite agreement with total GHGI livestock estimates, we find a significant increase in manure management emissions from 2.3 (1.9 - 2.8) Tg a<sup>-1</sup> to 3.1 (2.9 - 3.2) Tg a<sup>-1</sup>, which would almost entirely explain the observed discrepancy between the mean GHGI and posterior emissions. The increase in manure management emissions is concentrated over the California Central Valley, northern Iowa, and Sampson and Duplin Counties in North Carolina. California is home to more dairy cattle than any other state, Iowa is the largest pork-producing state, and Sampson and Duplin Counties are the two largest pork-producing counties in CONUS (USDA, 2019). We find no correlation between our inferred increase and dairy cattle or hog populations, which could reflect variability in manure management practices.

430

Posterior oil and gas emissions are 10.4 (10.1 - 10.7) Tg a<sup>-1</sup>, a 12% increase from the GHGI estimate of 9.3 (8.1 - 10.6) Tg a<sup>-1</sup>. Lu et al. (2022) found much larger posterior emissions of 4.8 (3.1 - 4.9) Tg a<sup>-1</sup> for oil and 8.9 (8.0 - 9.8) Tg a<sup>-1</sup> for gas in 2017, and Lu et al. (2023) used the same inversion framework to find even larger total oil and gas emissions of 15.6 (12.8 - 17.1) Tg a<sup>-1</sup> for 2019 driven by increased emissions in the Anadarko, Marcellus, Barnett, and Haynesville Shales. Although we find good agreement on average with the basin-level emissions from Lu et al. (2023), we find much smaller emissions in the Anadarko and Marcellus Shales, as shown in Fig. S4. This difference likely results in part from the use of lognormal prior errors in Lu et al. (2023). Compared to Lu et al. (2022, 2023), Worden et al. (2022) found smaller 2019 emissions in the United States for oil of  $2.4 \pm 0.3$  Tg a<sup>-1</sup> and for gas of  $7.9 \pm 0.9$  Tg a<sup>-1</sup>, and Shen et al. (2022) found oil and gas emissions of  $12.6 \pm 2.1$  Tg a<sup>-1</sup> from an inversion of TROPOMI data over 14 North American basins extrapolated to the national scale for May 2018 to February 2020. Both these emission estimates are within the uncertainty range of our posterior estimate. We also find consistent basin-level results with Shen et al. (2022) as shown in Fig. S4. Emissions for all posterior basins but one are within 0.25 Tg a<sup>-1</sup> of Shen et al. (2022) and all but six are within 0.10 Tg a<sup>-1</sup>. In particular, we find agreement within error bars in the Haynesville, Barnett, and Anadarko Shales. Of the basins where posterior emissions exceed the 0.5 Tg a<sup>-1</sup> threshold defined by Shen et al. (2022) for successful quantification of basin emissions by TROPOMI, we find significant differences only in the Permian basin, where we find smaller emissions of 2.8 (2.8 - 2.9) Tg a<sup>-1</sup>. Our Permian estimate is consistent within error

455 bars with Lu et al. (2023) and with other recent studies when basin extent differences are accounted for (Zhang et al., 2020; Schneising et al., 2020; Liu et al., 2021; Varon et al., 2022; McNorton et al., 2022; Veefkind et al., 2023).

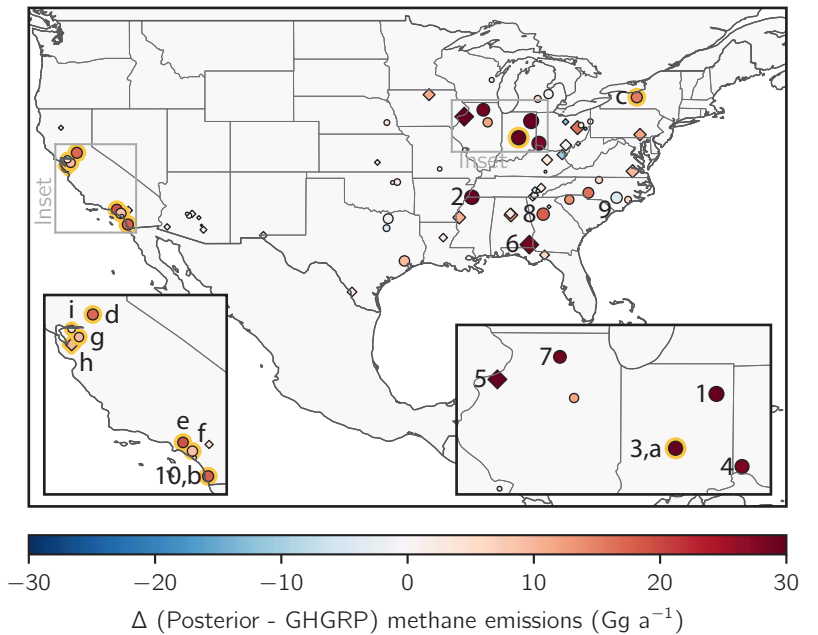
### 3.2 Landfill emissions

We consider in more detail the 51% increase in our posterior landfill emissions relative to the GHGI. GHGI landfill estimates scale up the total emissions reported to the GHGRP to account for non-reporting landfills (EPA, 2023a). The GHGRP reporting 460 requirements applied to 1297 landfills emitting more than 1 Gg  $a^{-1}$  across the U.S. in 2019 (EPA GHGRP, 2019), over 500 of which had gas recovery systems (EPA LMOP, 2019). The GHGRP requires that landfills use two methods to report emissions. Facilities without gas collection use two approaches that rely on landfill attributes and a first-order decay model based on landfilled mass so that emissions peak the year after waste disposal. However, a survey of 128 California landfills with gas 465 recovery systems found that methane was produced at relatively constant rates over time (Spokas et al., 2015). Landfills with gas collection use one of these methods with recovered methane removed from the modelled emissions in addition to a back-calculation approach that estimates emissions as a function of recovered methane given an estimated collection efficiency based on cover and operation methods. A default efficiency of 0.75 is assumed if cover information is unavailable (EPA, 2023a). Both the model and back-calculation methods have high uncertainties and have not been field validated (NAS, 2018).

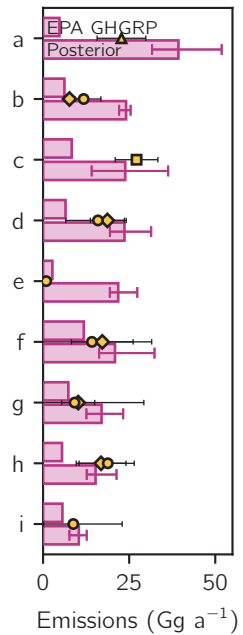
470 We compare our posterior landfill emissions to individual GHGRP facilities that reported more than 2.5 Gg  $a^{-1}$  methane in 2019. Of these 531 landfills, we limit our analysis to the 87  $0.25^\circ \times 0.3125^\circ$  grid cells where TROPOMI provides an averaging kernel sensitivity of at least 0.20 and where landfills explain at least 50% of prior emissions so that we are confident of our ability to separate landfill emissions from other sources. We exclude 33 facilities in grid cells containing multiple landfills because we are unable to separate the individual contributions to total emissions. Figure 5 shows the posterior emissions and 475 corrections to the GHGRP for the remaining 70 facilities, Table 3 shows GHGRP and posterior information for the top 10 methane-producing landfills as ranked by posterior emissions, and Table S3 shows GHGRP and posterior information for all 70 facilities.

We validate our posterior landfill results by comparison to aircraft-derived estimates for nine facilities as shown in Fig. 5. 480 Cambaliza et al. (2015), Smith (2021), and Catena et al. (2022) used mass balance approaches to estimate emissions using observations from 2011, 2019 to 2021, and November 2021, respectively. Duren et al. (2019) used the integrated methane enhancement method with data from 2016 to 2018. We find agreement within error bounds at the Seneca Meadows Landfill in New York (landfill c in Fig. 5; Catena et al., 2022) and at the Kiefer (d), Frank R. Bowerman (f), Altamont (g), Newby Island (h), and Keller Canyon (i) Landfills in California (Smith, 2021; Duren et al., 2019). We find much larger emissions than 485 previous studies at the South Side Landfill (a) in Indiana (Cambaliza et al., 2015) and at the West Miramar Sanitary (b) and Puente Hills (e) Landfills in California (Smith, 2021; Duren et al., 2019). The discrepancy at the South Side Landfill could

## Landfill methane emissions



## Validation



Posterior emissions	Validation site	Cambaliza et al. (2015)
◊ ◊ 10 $\text{Gg a}^{-1}$	○ Validation site	▴ ▴
◊ ◊ 20 $\text{Gg a}^{-1}$	○ Gas collected	◊ ◊
◊ ◊ 40 $\text{Gg a}^{-1}$	◊ Gas not collected	▪ ▪

**Figure 5:** Methane emissions for 2019 from 70 individual landfills that report methane emissions of  $2.5 \text{ Gg a}^{-1}$  or more to the EPA's Greenhouse Gas Reporting Program (GHGRP) for 2019 and for which our TROPOMI inversion provides site-specific information. The left panel shows the location of the landfills, with insets for parts of California (left) and Illinois and Indiana (right). Posterior emissions for each landfill are shown by the size of the marker. The colors show differences ( $\Delta$ ) between the posterior and GHGRP emissions for 2019, with red colors indicating posterior emissions larger than the reported value. Facilities that collect landfill gas are shown as circles, and others are shown as diamonds. The numbers (1 to 10) identify the top 10 methane-producing landfills listed in Table 3, and the letters (a to i) identify the nine validation sites listed in the right panel and outlined in gold. Validation sites are landfills with independent estimates from aircraft campaigns as listed in the legend. Cambaliza et al. (2015) based their estimates on data from 2011, Duren et al. (2019) on data from 2016 to 2018, Smith (2021) on data from 2019 to 2021, and Catena et al. (2022) on data from November 2021. The right panel shows GHGRP (top bars) and posterior (bottom bars) emissions for the validation sites, along with values reported from the aircraft campaigns. Sites are (a) South Side Landfill, (b) West Miramar Sanitary Landfill, (c) Seneca Meadows Landfill, (d) Kiefer Landfill, (e) Puente Hills Landfill, (f) Frank R. Bowerman Landfill, (g) Altamont Landfill, (h) Newby Island Landfill, and (i) Keller Canyon Landfill.

reflect changed emissions since 2011, including the construction of a large landfill gas recovery facility beginning in June 2019 (EPA LMOP, 2019). Methane concentrations of 8662 ppm were recorded at a leak at the West Miramar Sanitary Landfill in November 2019 (San Diego Air Pollution Control District, 2019), suggesting that estimates from other years may not be representative of 2019 emissions. The Puente Hills Landfill closed in 2013 but was previously one of the largest landfills in

**Table 3:** Top 10 methane-producing landfills in CONUS for 2019.

Facility <sup>1</sup>	Location	Emissions (Gg a <sup>-1</sup> )		Gas capture efficiency	
		GHGRP <sup>2</sup>	Posterior <sup>3</sup>	GHGRP <sup>4</sup>	Posterior <sup>5</sup>
1. National Serv-All Landfill	Fort Wayne, Indiana	3.4	44 (34 - 59)	0.86	0.32 (0.26 - 0.37)
2. South Shelby Landfill	Memphis, Tennessee	4.1	41 (30 - 56)	0.86	0.39 (0.31 - 0.46)
3. South Side Landfill Inc.	Indianapolis, Indiana	4.7	39 (32 - 52)	N/A	N/A
4. Rumpke Sanitary Landfill	Cincinnati, Ohio	10.1	39 (33 - 43)	0.84	0.58 (0.55 - 0.61)
5. Quad Cities Landfill Phase IV	Milan, Illinois	3.7	35 (28 - 47)	N/A	N/A
6. City of Dothan Sanitary Landfill	Dothan, Alabama	5.8	35 (28 - 43)	N/A	N/A
7. Rochelle Municipal Landfill	Rochelle, Illinois	2.7	32 (25 - 39)	0.76	0.22 (0.18 - 0.26)
8. Seminole Road MSW Landfill	Ellenwood, Georgia	12.3	30 (25 - 36)	0.18	0.08 (0.07 - 0.1)
9. Sampson County Disposal, LLC	Roseboro, North Carolina	29.2	25 (23 - 29)	0.37	0.41 (0.38 - 0.44)
10. West Miramar Sanitary Landfill	San Diego, California	6.2	24 (22 - 25)	0.78	0.47 (0.46 - 0.49)

<sup>1</sup>The top 10 landfills with the largest posterior methane emissions from the TROPOMI inversion for 2019. Numbers correspond to the labels in Fig. 5.

510 <sup>2</sup>Emissions reported by individual landfills to the EPA GHGRP for 2019 in gigagrams per year.

<sup>3</sup>Posterior emissions from the inversion of TROPOMI observations in gigagrams per year. Posterior emissions are allocated to individual facilities as described in Sects. 2.8 and 3.2. Values in parentheses represent the range from the eight-member inversion ensemble.

<sup>4</sup>For facilities that capture landfill gas, the recovery efficiency as calculated from emissions and recovered methane reported by individual landfills to the EPA LMOP. Facilities that do not capture landfill gas are listed as N/A.

515 <sup>5</sup>The posterior recovery efficiency as calculated from posterior emissions and the recovered methane reported by individual landfills to the EPA LMOP.

CONUS (EPA GHGRP, 2019). Our landfill attribution approach, which relies on a prior estimate from 2012, may therefore misallocate emissions to the Puente Hills Landfill instead of to co-located oil and gas operations.

520 We find mean facility emissions of 13 Gg a<sup>-1</sup> compared to the GHGRP mean of 7.2 Gg a<sup>-1</sup> for the 70 landfills considered here, with a median 77% increase in reported emissions. The largest increases occur for facilities that capture landfill gas, for which we find a median 204% increase from the reported values. As reflected in Table 3, we find no correlation ( $R^2 = 0.00$ ) between GHGRP emissions and our posterior estimates, which does not improve when we consider only facilities that do or do not capture landfill gas. This implies that the bottom-up approaches used for emissions estimation have little predictability.

525 For the 38 facilities that recover gas, we use captured methane emissions reported to the EPA Landfill Methane Outreach Program (LMOP) in 2019 together with posterior and GHGRP emissions to calculate a posterior and reported recovery efficiency, respectively. The average posterior recovery efficiency of 0.50 (0.33 - 0.54) is much smaller than the GHGRP mean of 0.61, and both are much smaller than the 0.75 default (EPA, 2023a). Across the six landfill gas facilities at the top 10 methane-producing landfills, we find a mean posterior recovery efficiency of 0.33 that is half the GHGRP value of 0.65.

Indeed, four of the six facilities report methane emission and recovery values consistent with efficiencies larger than the 0.75 default. We find a similar but still lower efficiency at the Seminole Road MSW Landfill (landfill 8) and a marginally higher recovery efficiency only at Sampson County Disposal, LLC (11). We find a low correlation ( $R^2 = 0.17$ ) between the efficiencies  
535 that does not depend on facility size but improves slightly for facilities constructed within the last decade ( $R^2 = 0.31$ ).

We consider in detail the 33 facilities for which posterior emissions show a significant 50% difference from the GHGRP. We  
540 find larger emissions for 28 of these facilities, with the largest discrepancies occurring in nine of the top 10 methane-producing landfills. Three of these nine facilities experienced significant operational changes in the last decade. The South Shelby (landfill 2 in Fig. 5) and South Side (3) Landfills constructed large landfill gas facilities in 2019 (EPA LMOP, 2019; Russell, 2019), suggesting that emissions from gas infrastructure development may be large. The City of Dothan Sanitary Landfill (6) has been full since 2014, when it stopped accepting most trash (Wise, 2019). Reported emissions peaked at  $7.4 \text{ Gg a}^{-1}$  that year (EPA GHGRP, 2019), a value almost five times smaller than our posterior emissions, suggesting that the first order decay model is inadequate to reproduce methane emissions over time. We also find a record of air quality and landfill standard  
545 violations at these 34 facilities. At the West Miramar Sanitary Landfill (10, b), a leak emitting 8662 ppm methane was recorded in November 2019 (San Diego Air Pollution Control District, 2019). The Sussex County Landfill in Virginia was fined USD 99000 in 2016 for failing to address cracks in the landfill cover (Vera, 2016). Lastly, the Newby Island Landfill (h), received 30 violation notices from 2014 to 2020, including for gas collection system shutdowns (Bay Area Air Quality Management District, 2022).

550 There are five facilities for which our posterior emissions are significantly smaller than the 2019 GHGRP by 50%. Three report large decreases in estimated methane emissions from 2019 to 2020 that result from changed methodology (EPA GHGRP, 2019). The updated estimates are consistent with our posterior emissions within error estimates in two cases and within 30% of our posterior emissions in the third case.

### 555 3.3 State emissions

The EPA recently began disaggregating the GHGI by state. The EPA uses the same methods to calculate state emissions as in the national inventory so that the total emissions are the same in both estimates. State estimates are developed without reference to greenhouse gas inventories prepared by state governments, which may result in discrepancies in sectoral or total values due to different methods or accounting (EPA, 2023b). In addition to the GHGI state estimates, the EPA provides references to the  
560 independent inventories of 24 states and Washington, D.C. (EPA, 2023). Of these, we find that eight produce a methane emission estimate separate from their inventory of total CO<sub>2</sub>-equivalent greenhouse gases.

## State emissions

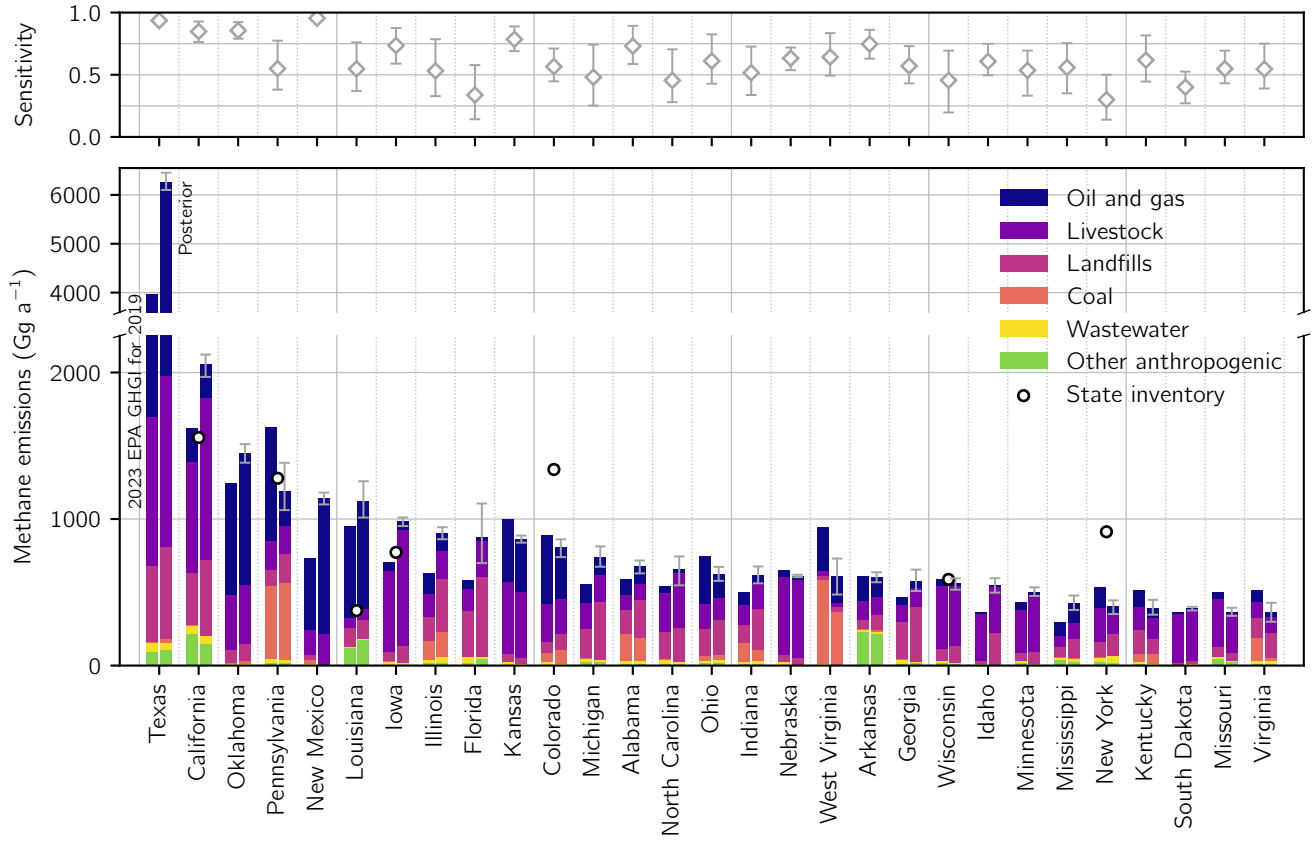


**Figure 6:** Anthropogenic methane emissions in 2019 for the 29 states responsible for 90% of U.S. anthropogenic posterior emissions. The bottom panel shows 2023 EPA GHGI state estimates for 2019 (left bar) and our posterior estimates from the inversion of TROPOMI data (right bar) divided by sector. States are listed from largest to smallest posterior emissions. The information content from the TROPOMI data as defined by the reduced-form averaging kernel sensitivities (the diagonal elements of the reduced-form averaging kernel matrix; Sect. 2.8) is shown in the top panel. Values of 1 indicate full sensitivity to TROPOMI, while values of 0 indicate no sensitivity. The error bars give the spread from the eight-member inversion ensemble. Also shown are emissions estimates from independent state inventories referenced by EPA (2022).

565

570 We partition our anthropogenic gridded posterior emission estimates, excluding offshore emissions, to each of the 48 states in CONUS as described in Sect. 2.8 and compare the results to the GHGI state estimates and to inventories prepared by state governments. Figure 6 shows the results for the 29 states responsible for 90% of posterior CONUS anthropogenic emissions excluding offshore emissions and ordered by posterior emissions, and Table S1 shows the full results for all 48 CONUS states. TROPOMI provides a strong constraint at this resolution, with most state averaging kernel sensitivities larger than 0.5. Our 575 state emissions are on average 7% larger than the GHGI estimates and 28% larger in the top 10 methane-emitting states, which produce 55% of CONUS posterior emissions. Oil and gas emissions on average generate 37% of posterior emissions and 48% of the observed increase relative to the GHGI in these 10 states. In Texas, Oklahoma, New Mexico, and Louisiana, the oil and gas sector explains more than 60% of posterior emissions, with emissions concentrated in the Permian Basin, the Haynesville

Shale, and the Anadarko Shale. Livestock and landfills also play a significant role in these states. Emissions in California and  
580 Iowa are dominated by the livestock sector, with much of the observed increase relative to the GHGI attributed to manure management emissions (Sect. 3.1). Landfills account for 41% of posterior emissions in Illinois and 62% in Florida. Indeed, three of the ten largest landfills as reported to the GHGRP in 2019 are in Florida (EPA GHGRP, 2019). Consistent with our sectoral analysis, the largest posterior emission decreases relative to the GHGI are found in coal-producing states, including West Virginia and Pennsylvania. While we find a large decrease compared to the GHGI in Pennsylvania, we cannot confidently  
585 attribute the difference to a specific sector due to co-location of oil, gas, and coal facilities at the resolution of our inversion.

We consider in more detail Texas and California, which are responsible for 21% and 7% of posterior CONUS anthropogenic emissions, respectively. Our posterior estimate for Texas is  $6.3 (6.1 - 6.5) \text{ Tg a}^{-1}$ , a 58% increase from the GHGI estimate of  $4.0 \text{ Tg a}^{-1}$ . This increase is attributed almost entirely to the oil and gas sector, which accounts for 69% of posterior emissions  
590 compared to 57% in the GHGI. The Permian basin alone explains almost 40% of Texas' posterior emissions. In California, we find posterior emissions of  $2.1 (2.0 - 2.1) \text{ Tg a}^{-1}$ , 53% of which occur in the San Joaquin Valley air basin. Our posterior emissions increase 27% from the GHGI estimate of  $1.6 \text{ Tg a}^{-1}$  and 34% from an independent estimate produced by CARB of  $1.5 \text{ Tg a}^{-1}$  (CARB, 2023). Our posterior estimate is smaller than but consistent within error bars with a value of  $2.4 \pm 0.5 \text{ Tg a}^{-1}$  found by an inversion of in situ observations in California from June 2013 to May 2014 (Jeong et al., 2016). We find in  
595 general good agreement with the sectoral partitioning in the GHGI22, the CARB inventory, and Jeong et al. (2016). Livestock explain 54% of emissions in our posterior estimate, 47% in the GHGI, 55% in the CARB inventory, and 54% in Jeong et al. (2016), while landfills explain 25%, 22%, 21%, and 19% of emissions, respectively. We find slightly smaller relative contributions from oil and gas, which accounts for 11% of emissions in our posterior estimate compared to 14%, 17%, and 18% in the GHGI, the CARB inventory, and Jeong et al. (2016), respectively. This partitioning differs from that found in an  
600 inversion of the 2010 CalNex aircraft campaign observations, where 30% of emissions were attributed to livestock, 38% to landfills, and 22% to oil and gas based on the sectoral distribution of the EDGAR v4.2 methane emission inventory (Wecht et al., 2014b).

We also compare our posterior emissions to independent state greenhouse gas inventories from Pennsylvania, Louisiana, Iowa,  
605 and Colorado referenced by EPA (2023), where we have a strong constraint from the inversion (state averaging kernel sensitivity greater than 0.5). Our posterior agrees with the Pennsylvania estimate (Pennsylvania DEP, 2022), but we find a source shift from fossil fuels (from 76% in the inventory to 63% in our work) to landfills (from 3% in the inventory to 16% in our work). We find that Louisiana's state inventory (Dismukes, 2021) is too low due to underestimated oil and gas emissions, while Iowa's (Iowa DNR, 2020) is too low due to underestimated livestock emissions, particularly from manure management  
610 (Sect. 3.1). Colorado's state inventory (Taylor, 2021) is 65% larger than our posterior estimate due to oil and gas emissions that are more than twice as large.

### 3.4 Urban area emissions

Urban areas are home to 81% of the U.S. population (U.S. Census Bureau, 2010) and are major sources of greenhouse gas emissions, including methane (Gurney et al., 2015; Hopkins et al., 2016). As urban populations grow (Seto et al., 2012), these

615 emissions are likely to increase. Cities are well positioned to address methane emissions through waste-reduction initiatives, leak-detection programs, and strategic contracts with landfill operators and gas utilities. Regulation by air pollution control districts can also aid urban emissions reduction efforts (Hopkins et al., 2016). C40, a performance-based coalition of over 100 mayors dedicated to climate change mitigation, recommends that cities target a 50% reduction in methane emissions by 2030 (C40, 2022b). Numerous cities, including New York City, Los Angeles, and Philadelphia, are working toward these reductions  
620 through zero-waste programs (C40, 2022a). The U.S. Methane Emissions Reduction Action Plan intends to work with local governments to set up methane monitoring systems to identify and publicize information about municipal gas distribution leaks. The plan also challenges members of the U.S. Climate Mayors to prioritize pipeline abandonment or replacement (The White House, 2021).

625 We calculate posterior emissions for 95 urban areas across CONUS with 2010 populations over 1 million and averaging kernel sensitivities from our inversion greater than 0.2, providing the first comprehensive national analysis of urban methane emissions. Quantification of urban emissions depends significantly on the definition of city extent due to the presence of large emitters such as landfills on the urban periphery (e.g., Balashov et al., 2020; Plant et al., 2022). We follow Plant et al. (2022)  
630 and others in using the U.S. Census Topographically Integrated Geographic Encoding and Referencing system (TIGER)/Line Urban Areas to standardize the definition across CONUS (U.S. Census Bureau, 2017). These urban areas are responsible for almost a quarter of the GHGI23 emissions spatially allocated using the gridded inventory from Maasakkers et al. (2016). The gridded inventory does not include post-meter emissions introduced in later versions of the GHGI, which we distribute by population for this analysis. In an average city, the gridded GHGI emissions originate from landfills (40%), gas distribution (9%, including 4% from post-meter emissions), wastewater (6%), and other sources that are not specific to urban areas such  
635 as livestock and oil and gas production and transmission (45%).

Anthropogenic posterior emissions in these 95 urban areas total  $6.0\ (5.4 - 6.7)\ \text{Tg}\ \text{a}^{-1}$ , 38 (24 - 54) % larger than the gridded GHGI23 value of  $4.3\ \text{Tg}\ \text{a}^{-1}$ . Individual urban area emissions, listed in Table S2, increase by an average of 39 (27 - 52) %. These increases are much larger than the 13% increase we find in total CONUS anthropogenic emissions relative to the  
640 GHGI23. We are unable to attribute the increased emissions to individual sectors due to source co-location within urban areas at the  $0.25^\circ \times 0.3125^\circ$  resolution of our inversion. However, given that landfills account for 40% of gridded GHGI23 emissions in an average urban area and increase 51% relative to the GHGI23, it is likely that they are responsible for a large fraction of

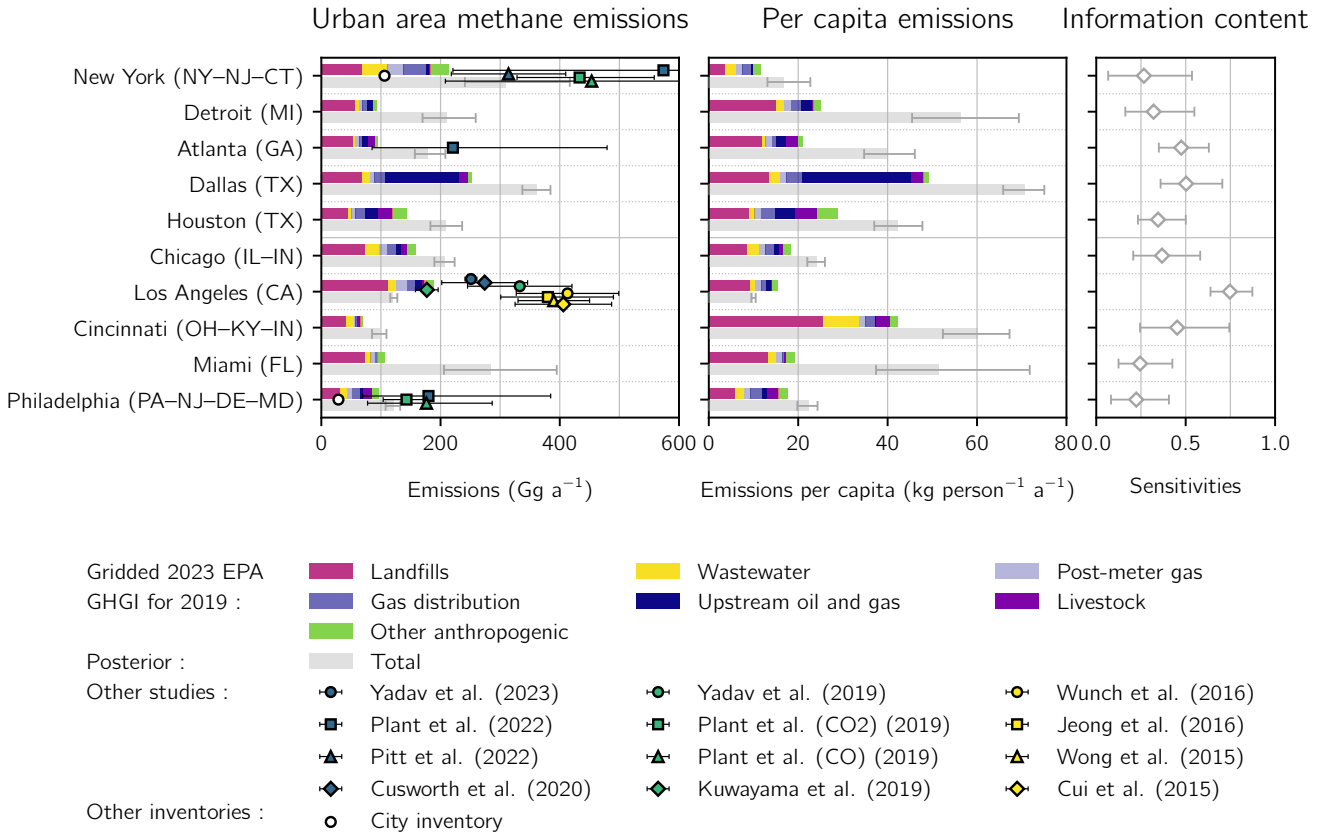


**Figure 7:** Anthropogenic methane emissions for the largest 10 methane-producing urban areas in the contiguous United States (CONUS) for 2019 as identified by the inversion of TROPOMI data. Urban area extents are given by the U.S. Census Bureau TIGER/Line files (U.S. Census, 2010). The top bars show prior anthropogenic sectoral emissions from the 2023 EPA GHGI for 2019 spatially allocated following Maasakkers et al. (2016) with post-meter emissions allocated by population. The bottom bar shows posterior emissions from the TROPOMI inversion for 2019. We do not resolve posterior sectoral emissions estimates due to source colocation within urban areas at the scale of the inversion. Total emissions (left panel), per capita emissions (center panel), and averaging kernel sensitivities (right panel) are shown for each urban area. Error bars represent the spread of the eight-member inversion ensemble. Also shown are independent urban emissions estimates.

the observed discrepancy. It is also likely that gas emissions, which represent less than 20% of gridded GHGI23 emissions in an average urban area but explain between 32% and 100% of methane emissions in many cities based on field measurements of methane-ethane ratios (Plant et al., 2019; Floerchinger et al., 2021; Sargent et al., 2021), are significantly underestimated.

Finally, recent studies have shown large underestimates of methane emissions from wastewater treatment in the GHGI (Moore et al., 2023; Song et al., 2023) and over urban areas (de Foy et al., 2023), but increasing wastewater emissions accordingly only accounts for 2% of our observed discrepancy. City-specific variability prevents further attribution of urban emissions. Indeed, we find no correlation between the posterior emission increase and urban area population, population change from 2000 to 2010, population density, or surface area.

Figure 7 shows results for the top 10 methane-producing urban areas as ranked by posterior emissions from landfills, gas distribution, and wastewater. These 10 regions explain 35 (34 - 36) % of anthropogenic posterior emissions across the 95 urban areas considered here. We find a mean increase relative to gridded GHGII23 emissions of 58 (37 - 84) %. We also compare our posterior emissions to municipal inventories from New York City and Philadelphia, the only available bottom-up urban methane emission estimates. Our emissions are more than twice as large as these inventories, but this likely results from our consideration of broader urban areas.

Figure 7 also compares our results to 12 top-down studies published since 2015. Most of these focused on New York City or Los Angeles. Almost all the studies used larger definitions of urban area extent, with only Pitt et al. (2022) and Plant et al. (2022) using the U.S. Census designation. Most used aircraft or tower observations to infer emissions by inverting a CTM (Cui et al., 2015; Jeong et al., 2016; Cusworth et al., 2020; Pitt et al., 2022; Yadav et al., 2019, 2023). Kuwayama et al. (2019) used a mass balance approach, while others used observed methane to CO<sub>2</sub> or CO ratios together with bottom-up inventories of these gases (Wong et al., 2015; Wunch et al., 2016; Plant et al., 2019). Plant et al. (2022) used the same approach with TROPOMI methane to CO emissions.

675

We find in general lower but statistically consistent emissions compared to these studies. Our smaller estimates likely result from our restrictive definition of urban area extent. The only study that used aircraft data to estimate emissions within a U.S. Census Urban Area found  $314 \pm 96 \text{ Gg a}^{-1}$  in New York City (Pitt et al., 2022), which is very similar to our estimate of 309 (241 - 417) Gg a<sup>-1</sup>. Plant et al. (2022) used U.S. Census Urban Areas but relied on TROPOMI methane to CO ratios. They 680 found slightly larger emissions in Atlanta and Philadelphia and much larger emissions in New York City, but their error bars spanned ranges almost twice as large as the derived emissions, limiting the utility of the comparison. Plant et al. (2019) found larger emissions in New York City and Philadelphia but used larger definitions of urban areas and produced similarly wide error ranges.

685 We find much lower emissions than these studies only in Los Angeles, a difference that decreases but remains significant when we use the same extent as these studies. We attribute much of the discrepancy to decreasing emissions over time. Methane emissions from the Puente Hills Landfill, previously one of the largest landfills in CONUS, decreased following its closure in 2013 (Yadav et al., 2019). This change is not fully reflected in the estimates of Cui et al. (2015), Wong et al. (2015), or Wunch et al. (2016). Yadav et al. (2023) found that Los Angeles emissions decreased an additional 7% from January 2015 to May 690 2020. However, their posterior estimate of  $251 \pm 5 \text{ Gg a}^{-1}$  for 2019 is still larger than our value of 179 (171 - 193) Gg a<sup>-1</sup>.

## 4 Conclusions

We used TROPOMI atmospheric methane column observations for 2019 to optimize methane emissions at  $0.25^\circ \times 0.3125^\circ$  resolution over North America with a focus on the contiguous U.S. (CONUS). The high resolution of our inversion allowed us to quantify emissions from individual landfills, states, and urban areas. We compared our results to the 2023 EPA

695 Greenhouse Gas Emissions Inventory (GHGI), including state-level estimates, for 2019; to emissions reported by individual landfills to the EPA Greenhouse Gas Reporting Program (GHGRP); and to other estimates from states and cities. We find large upward corrections to the GHGI at all scales, which may present a challenge for U.S. climate policies and goals, many of which target significant reductions in methane emissions.

700 We optimized methane emissions using an analytical inversion of TROPOMI methane observations with the GEOS-Chem chemical transport model run at  $0.25^\circ \times 0.3125^\circ$  resolution. The inverse solution, or posterior emission estimate, was obtained through a reduced-rank approximation of the analytical minimum of a Bayesian cost function regularized by a prior emission estimate from a gridded version of the GHGI. The analytical solution characterizes the error and information content of the posterior emissions and supported the generation of an eight-member inversion ensemble. We constructed the Jacobian matrix

705 required for the high-resolution, continent-scale analytical solution by iterative approximation using the emissions patterns best informed by the prior emission estimate and the observations. This approach decreases the computational cost of our inversion by an order of magnitude compared to conventional analytical methods while optimally preserving its information content.

710 We find posterior anthropogenic methane emissions of 30.9 (30.0 - 31.8) Tg  $a^{-1}$  in CONUS, where the range is given by the inversion ensemble. This is a 13% increase from the GHGI estimate of 27.3 (25.1 - 30.6) Tg  $a^{-1}$ , where the range is given by the 95% confidence interval. Emissions for landfills, oil and gas, and livestock explain 89% of posterior CONUS emissions and each of these sectors' emissions increase by at least 10% relative to the GHGI. We find a significant decrease compared to the 2023 GHGI only for coal emissions. These increases present a challenge to goals set by the U.S. government to decrease  
715 methane emissions from oil and gas, livestock, and landfills.

Most of the total increase from the GHGI to the posterior emissions is attributed to a 51% increase in landfill emissions. We compare our optimized emissions for 70 individual landfills to those reported to the GHGRP and find a median 77% increase in emissions relative to reported values. We attribute the underestimated GHGI and GHGRP landfill emissions to standard  
720 inventory methods that (1) assume too-high recovery efficiencies at facilities that collect landfill gas and (2) inadequately account for anomalous operating events such as gas leaks or the construction of new landfill gas facilities.

We took advantage of the high resolution of our inversion to quantify emissions for each of the 48 states in CONUS and compare to the newly available state emission inventories published most recently with the 2022 GHGI. We find a 7% average  
725 increase with a 27% average increase in the top 10 methane-emitting states. Much of the discrepancy in these 10 states is attributed to increased oil and gas emissions, though livestock and landfills also play significant roles. Texas and California, the two largest methane-producing states, respectively emit 21% and 7% of total CONUS anthropogenic emissions in our posterior estimate. Emissions in Texas increase by 58% relative to the GHGI almost entirely due to the oil and gas sector.  
730 Operations in the Permian basin alone explain almost 40% of all posterior emissions in the state. In California, we find a 27% increase from the GHGI and a 34% increase from an independent inventory prepared by the California Air Resources Board (CARB). Our sectoral partitioning for California is consistent with both inventories, including 54% of emissions from livestock, 25% from landfills, and 11% from oil and gas.

We also provide a first national analysis of urban methane emissions by calculating emissions for 95 urban areas across  
735 CONUS. We find total emissions of 6.0 (5.4 - 6.7) Tg a<sup>-1</sup> across these urban areas, representing a fifth of posterior anthropogenic emissions in CONUS and a 38 (24 - 54) % increase from the gridded 2023 GHGI value of 4.3 Tg a<sup>-1</sup>. Urban emissions increase on average by 39 (27 - 52) % compared to the GHGI. We attribute the observed discrepancy to underestimated landfill and gas emissions. Our urban emission estimates are in general consistent with previous top-down studies except for Los Angeles, which may be attributable in part to decreasing emissions between study periods.

#### 740 **Code availability**

The GEOS-Chem code is available at <https://doi.org/10.5281/zenodo.3676008>, and the description of the model is available at [geos-chem.org](http://geos-chem.org). The code to solve and analyze the inversion is at [https://github.com/hannahesser/TROPOMI\\_inversion](https://github.com/hannahesser/TROPOMI_inversion).

#### **Data availability**

The TROPOMI v14 data are available from SRON at [https://ftp.sron.nl/open-access-data-2/TROPOMI/tropomi/ch4/14\\_14\\_Lorente\\_et\\_al\\_2020\\_AMTD/](https://ftp.sron.nl/open-access-data-2/TROPOMI/tropomi/ch4/14_14_Lorente_et_al_2020_AMTD/) (last access: 19 March 2021). The GLOBALVIEWplus CH<sub>4</sub>  
745 ObsPack v3.0 database is available from NOAA's Global Monitoring Laboratory at <http://dx.doi.org/10.15138/G3CW4Q>. The prior and observational inputs for the inversion, the posterior emissions and averaging kernel sensitivities, and summary datasets for sectors, states, cities, and landfills are available at [https://github.com/hannahesser/TROPOMI\\_inversion](https://github.com/hannahesser/TROPOMI_inversion). Additional data related to this paper may be requested from the authors.

## 750 Author contribution

HN and DJJ designed the study. HN conducted the inversion with contributions from ZC, ZQ, MPS, and MW. SM and AAB provided the high-performance ensemble of WetCHARTS v1.3.1 and supported wetland analysis. JDM and AL provided guidance on the TROPOMI data. JDM, AL, XL, LS, JW, RNS, and CAR discussed the results. HN and DJJ wrote the paper with input from all authors.

## 755 Competing interests

The contact author has declared that none of the authors has any competing interests.

## Acknowledgments

This work was supported by the NASA Carbon Monitoring System (CMS), ExxonMobil Technology and Engineering Company, and the Harvard Climate Change Solutions Fund. Part of this work was carried out at the Jet Propulsion Laboratory, 760 California Institute of Technology, under a contract with the National Aeronautics and Space Administration (NASA). We thank Bryan Mignone, Felipe J. Cardoso-Saldaña, Robert Stowe, Lauren Aepli, and Melissa Weitz for helpful discussions.

## References

- Balashov, N. V., Davis, K. J., Miles, N. L., Lauvaux, T., Richardson, S. J., Barkley, Z. R., and Bonin, T. A.: Background heterogeneity and other uncertainties in estimating urban methane flux: results from the Indianapolis Flux Experiment (INFLUX), *Atmospheric Chemistry and Physics*, 20, 4545–4559, <https://doi.org/10.5194/acp-20-4545-2020>, 2020.
- Balasus, N., Jacob, D. J., Lorente, A., Maasakkers, J. D., Parker, R. J., Boesch, H., Chen, Z., Kelp, M. M., Nesser, H., and Varon, D. J.: A blended TROPOMI+GOSAT satellite data product for atmospheric methane using machine learning to correct retrieval biases, *Atmospheric Measurement Techniques Discussions*, 1–40, <https://doi.org/10.5194/amt-2023-47>, 2023.
- Barré, J., Aben, I., Agustí-Panareda, A., Balsamo, G., Bouscerez, N., Dueben, P., Engelen, R., Inness, A., Lorente, A., McNorton, J., Peuch, V.-H., Radnoti, G., and Ribas, R.: Systematic detection of local CH<sub>4</sub> anomalies by combining satellite measurements with high-resolution forecasts, *Atmospheric Chemistry and Physics*, 21, 5117–5136, <https://doi.org/10.5194/acp-21-5117-2021>, 2021.
- Bay Area Air Quality Management District: Air District settles violations at Newby Island Landfill, 2022.
- Bloom, A. A., Bowman, K. W., Lee, M., Turner, A. J., Schroeder, R., Worden, J. R., Weidner, R., McDonald, K. C., and Jacob, D. J.: A global wetland methane emissions and uncertainty dataset for atmospheric chemical transport models (WetCHARTs version 1.0), *Geoscientific Model Development*, 10, 2141–2156, <https://doi.org/10.5194/gmd-10-2141-2017>, 2017.

Bousserez, N. and Henze, D. K.: Optimal and scalable methods to approximate the solutions of large-scale Bayesian problems: theory and application to atmospheric inversion and data assimilation, *Quarterly Journal of the Royal Meteorological Society*, 144, 365–390, <https://doi.org/10.1002/qj.3209>, 2018.

Brasseur, G. P. and Jacob, D. J.: Inverse Modeling for Atmospheric Chemistry, in: *Modeling of Atmospheric Chemistry*, Cambridge University Press, Cambridge, 487–537, <https://doi.org/10.1017/9781316544754.012>, 2017.

C40: C40 Advancing towards zero waste declaration: How cities are creating cleaner, healthier communities and circular economies, C40, 2022a.

785 C40: Methane: Why cities must act now, C40 Knowledge, July, 2022b.

Calisesi, Y., Soebijanta, V. T., and van Oss, R.: Regridding of remote soundings: Formulation and application to ozone profile comparison, *Journal of Geophysical Research: Atmospheres*, 110, <https://doi.org/10.1029/2005JD006122>, 2005.

790 Cambaliza, M. O. L., Shepson, P. B., Bogner, J., Caulton, D. R., Stirm, B., Sweeney, C., Montzka, S. A., Gurney, K. R., Spokas, K., Salmon, O. E., Lavoie, T. N., Hendricks, A., Mays, K., Turnbull, J., Miller, B. R., Lauvaux, T., Davis, K., Karion, A., Moser, B., Miller, C., Obermeyer, C., Whetstone, J., Prasad, K., Miles, N., and Richardson, S.: Quantification and source apportionment of the methane emission flux from the city of Indianapolis, *Elementa: Science of the Anthropocene*, 3, 000037, <https://doi.org/10.12952/journal.elementa.000037>, 2015.

CARB: Current California GHG Emission Inventory Data, 2023.

795 Catena, A. M., Zhang, J., Commane, R., Murray, L. T., Schwab, M. J., Leibensperger, E. M., Marto, J., Smith, M. L., and Schwab, J. J.: Hydrogen Sulfide Emission Properties from Two Large Landfills in New York State, *Atmosphere*, 13, 1251, <https://doi.org/10.3390/atmos13081251>, 2022.

Chen, Y., Sherwin, E. D., Berman, E. S. F., Jones, B. B., Gordon, M. P., Wetherley, E. B., Kort, E. A., and Brandt, A. R.: Quantifying Regional Methane Emissions in the New Mexico Permian Basin with a Comprehensive Aerial Survey, *Environ. Sci. Technol.*, 56, 4317–4323, <https://doi.org/10.1021/acs.est.1c06458>, 2022.

800 Chen, Z., Griffis, T. J., Baker, J. M., Millet, D. B., Wood, J. D., Dlugokencky, E. J., Andrews, A. E., Sweeney, C., Hu, C., and Kolka, R. K.: Source Partitioning of Methane Emissions and its Seasonality in the U.S. Midwest, *Journal of Geophysical Research: Biogeosciences*, 123, 646–659, <https://doi.org/10.1002/2017JG004356>, 2018.

Chevallier, F.: Impact of correlated observation errors on inverted CO<sub>2</sub> surface fluxes from OCO measurements, *Geophysical Research Letters*, 34, <https://doi.org/10.1029/2007GL030463>, 2007.

805 Cooperative Global Atmospheric Data Integration Project: Multi-laboratory compilation of atmospheric methane data for the period 1957–2017, NOAA Earth System Research Laboratory, Global Monitoring Laboratory, 2019.

810 Cui, Y. Y., Brioude, J., McKeen, S. A., Angevine, W. M., Kim, S.-W., Frost, G. J., Ahmadov, R., Peischl, J., Bousserez, N., Liu, Z., Ryerson, T. B., Wofsy, S. C., Santoni, G. W., Kort, E. A., Fischer, M. L., and Trainer, M.: Top-down estimate of methane emissions in California using a mesoscale inverse modeling technique: The South Coast Air Basin, *Journal of Geophysical Research: Atmospheres*, 120, 6698–6711, <https://doi.org/10.1002/2014JD023002>, 2015.

Cusworth, D. H., Duren, R. M., Yadav, V., Thorpe, A. K., Verhulst, K., Sander, S., Hopkins, F., Rafiq, T., and Miller, C. E.: Synthesis of Methane Observations Across Scales: Strategies for Deploying a Multitiered Observing Network, *Geophysical Research Letters*, 47, e2020GL087869, <https://doi.org/10.1029/2020GL087869>, 2020.

- 815 Deng, Z., Ciais, P., Tzompa-Sosa, Z. A., Saunois, M., Qiu, C., Tan, C., Sun, T., Ke, P., Cui, Y., Tanaka, K., Lin, X., Thompson, R. L., Tian, H., Yao, Y., Huang, Y., Lauerwald, R., Jain, A. K., Xu, X., Bastos, A., Sitch, S., Palmer, P. I., Lauvaux, T., d'Aspremont, A., Giron, C., Benoit, A., Poulter, B., Chang, J., Petrescu, A. M. R., Davis, S. J., Liu, Z., Grassi, G., Albergel, C., Tubiello, F. N., Perugini, L., Peters, W., and Chevallier, F.: Comparing national greenhouse gas budgets reported in UNFCCC inventories against atmospheric inversions, *Earth System Science Data*, 14, 1639–1675, 820 <https://doi.org/10.5194/essd-14-1639-2022>, 2022.
- Dismukes, D. E.: Louisiana 2021 Greenhouse Gas Inventory, Louisiana Governor's Office of Coastal Activities, 2021.
- Duren, R. M., Thorpe, A. K., Foster, K. T., Rafiq, T., Hopkins, F. M., Yadav, V., Bue, B. D., Thompson, D. R., Conley, S., Colombi, N. K., Frankenberg, C., McCubbin, I. B., Eastwood, M. L., Falk, M., Herner, J. D., Croes, B. E., Green, R. O., and Miller, C. E.: California's methane super-emitters, *Nature*, <https://doi.org/10.1038/s41586-019-1720-3>, 2019.
- 825 EIA: Annual Coal Report 2020, U.S. Energy Information Administration, 2021.
- EPA: <https://www.epa.gov/ghgemissions/learn-more-about-official-state-greenhouse-gas-inventories>, last access: 1 January 2023.
- EPA: Inventory of U.S. Greenhouse Gas Emissions and Sinks: 1990-2021., U.S. Environmental Protection Agency, 2023a.
- EPA: Methodology Report for Inventory of U.S. Greenhouse Gas Emissions and Sinks by State: 1990–2021, EPA-430-R-23-830 003, 2023b.
- EPA GHGRP: Facility Level Information on GreenHouse Gases Tool (FLIGHT), U.S. Environmental Protection Agency Greenhouse Gas Reporting Program, 2019.
- EPA LMOP: Landfill Methane Outreach Program (LMOP) Historical Database, U.S. Environmental Protection Agency Landfill Methane Outreach Program, 2019.
- 835 Floerchinger, C., Shepson, P. B., Hajny, K., Daube, B. C., Stirm, B. H., Sweeney, C., and Wofsy, S. C.: Relative flux measurements of biogenic and natural gas-derived methane for seven U.S. cities, *Elementa: Science of the Anthropocene*, 9, 000119, <https://doi.org/10.1525/elementa.2021.000119>, 2021.
- de Foy, B., Schauer, J. J., Lorente, A., and Borsdorff, T.: Investigating high methane emissions from urban areas detected by TROPOMI and their association with untreated wastewater, *Environ. Res. Lett.*, 18, 044004, <https://doi.org/10.1088/1748-9326/acc118>, 2023.
- 840 About the Global Methane Pledge: <https://www.globalmethanepledge.org/>, last access: 12 April 2023.
- de Gouw, J. A., Veefkind, J. P., Roosenbrand, E., Dix, B., Lin, J. C., Landgraf, J., and Levelt, P. F.: Daily Satellite Observations of Methane from Oil and Gas Production Regions in the United States, *Sci Rep*, 10, 1379, <https://doi.org/10.1038/s41598-020-57678-4>, 2020.
- 845 Gurney, K. R., Romero-Lankao, P., Seto, K. C., Hutyra, L. R., Duren, R., Kennedy, C., Grimm, N. B., Ehleringer, J. R., Marcotullio, P., Hughes, S., Pincetl, S., Chester, M. V., Runfola, D. M., Feddema, J. J., and Sperling, J.: Climate change: Track urban emissions on a human scale, *Nature*, 525, 179–181, <https://doi.org/10.1038/525179a>, 2015.

Hasekamp, O., Lorente, A., Hu, H., Butz, A., Aan de Brugh, J., and Landgraf, J.: Algorithm Theoretical Baseline Document for Sentinel-5 Precursor Methane Retrieval, 1, 1–67, 2019.

850 Heald, C. L., Jacob, D. J., Jones, D. B. A., Palmer, P. I., Logan, J. A., Streets, D. G., Sachse, G. W., Gille, J. C., Hoffman, R. N., and Nehrkorn, T.: Comparative inverse analysis of satellite (MOPITT) and aircraft (TRACE-P) observations to estimate Asian sources of carbon monoxide, *Journal of Geophysical Research D: Atmospheres*, 109, 1–17, <https://doi.org/10.1029/2004JD005185>, 2004.

855 Hopkins, F. M., Ehleringer, J. R., Bush, S. E., Duren, R. M., Miller, C. E., Lai, C.-T., Hsu, Y.-K., Carranza, V., and Randerson, J. T.: Mitigation of methane emissions in cities: How new measurements and partnerships can contribute to emissions reduction strategies, *Earth's Future*, 4, 408–425, <https://doi.org/10.1002/2016EF000381>, 2016.

860 Houweling, S., Krol, M., Bergamaschi, P., Frankenberg, C., Dlugokencky, E. J., Morino, I., Notholt, J., Sherlock, V., Wunch, D., Beck, V., Gerbig, C., Chen, H., Kort, E. A., Röckmann, T., and Aben, I.: A multi-year methane inversion using SCIAMACHY, accounting for systematic errors using TCCON measurements, *Atmospheric Chemistry and Physics*, 14, 3991–4012, <https://doi.org/10.5194/acp-14-3991-2014>, 2014.

Hu, H., Landgraf, J., Detmers, R., Borsdorff, T., Aan de Brugh, J., Aben, I., Butz, A., and Hasekamp, O.: Toward Global Mapping of Methane With TROPOMI: First Results and Intersatellite Comparison to GOSAT, *Geophysical Research Letters*, 45, 3682–3689, <https://doi.org/10.1002/2018gl077259>, 2018.

Iowa DNR: 2019 Iowa Statewide Greenhouse Gas Emissions Inventory Report, Iowa Department of Natural Resources, 2020.

865 IPCC: Global Warming of 1.5°C: IPCC Special Report on Impacts of Global Warming of 1.5°C above Pre-industrial Levels in Context of Strengthening Response to Climate Change, Sustainable Development, and Efforts to Eradicate Poverty, 1st ed., Cambridge University Press, <https://doi.org/10.1017/9781009157940>, 2022.

870 Jacob, D. J., Varon, D. J., Cusworth, D. H., Dennison, P. E., Frankenberg, C., Gautam, R., Guanter, L., Kelley, J., McKeever, J., Ott, L. E., Poulter, B., Qu, Z., Thorpe, A. K., Worden, J. R., and Duren, R. M.: Quantifying methane emissions from the global scale down to point sources using satellite observations of atmospheric methane, *Atmospheric Chemistry and Physics*, 22, 9617–9646, <https://doi.org/10.5194/acp-22-9617-2022>, 2022.

875 Janssens-Maenhout, G., Crippa, M., Guizzardi, D., Muntean, M., Schaaf, E., Dentener, F., Bergamaschi, P., Pagliari, V., Olivier, J. G. J., Peters, J. A. H. W., van Aardenne, J. A., Monni, S., Doering, U., Petrescu, A. M. R., Solazzo, E., and Oreggioni, G. D.: EDGAR v4.3.2 Global Atlas of the three major greenhouse gas emissions for the period 1970–2012, *Earth System Science Data*, 11, 959–1002, <https://doi.org/10.5194/essd-11-959-2019>, 2019.

Jeong, S., Newman, S., Zhang, J., Andrews, A. E., Bianco, L., Bagley, J., Cui, X., Graven, H., Kim, J., Salameh, P., LaFranchi, B. W., Priest, C., Campos-Pineda, M., Novakovskia, E., Sloop, C. D., Michelsen, H. A., Bambha, R. P., Weiss, R. F., Keeling, R., and Fischer, M. L.: Estimating methane emissions in California's urban and rural regions using multitower observations, *Journal of Geophysical Research: Atmospheres*, 121, 13,031–13,049, <https://doi.org/10.1002/2016JD025404>, 2016.

880 Karion, A., Sweeney, C., Kort, E. A., Shepson, P. B., Brewer, A., Cambaliza, M., Conley, S. A., Davis, K., Deng, A., Hardesty, M., Herndon, S. C., Lauvaux, T., Lavoie, T., Lyon, D., Newberger, T., Pétron, G., Rella, C., Smith, M., Wolter, S., Yacovitch, T. I., and Tans, P.: Aircraft-Based Estimate of Total Methane Emissions from the Barnett Shale Region, *Environ. Sci. Technol.*, 49, 8124–8131, <https://doi.org/10.1021/acs.est.5b00217>, 2015.

885 Konan, D. E. and Chan, H. L.: Greenhouse gas emissions in Hawai‘i: Household and visitor expenditure analysis, *Energy Economics*, 32, 210–219, <https://doi.org/10.1016/j.eneco.2009.06.015>, 2010.

Kuwayama, T., Charrier-Klobas, J. G., Chen, Y., Vizenor, N. M., Blake, D. R., Pongetti, T., Conley, S. A., Sander, S. P., Croes, B., and Herner, J. D.: Source Apportionment of Ambient Methane Enhancements in Los Angeles, California, To Evaluate Emission Inventory Estimates, *Environ Sci Technol*, 53, 2961–2970, <https://doi.org/10.1021/acs.est.8b02307>, 2019.

Liu, M., van der A, R., van Weele, M., Eskes, H., Lu, X., Veefkind, P., de Laat, J., Kong, H., Wang, J., Sun, J., Ding, J., Zhao, Y., and Weng, H.: A New Divergence Method to Quantify Methane Emissions Using Observations of Sentinel-5P TROPOMI, *Geophysical Research Letters*, 48, e2021GL094151, <https://doi.org/10.1029/2021GL094151>, 2021.

Lorente, A., Borsdorff, T., Butz, A., Hasekamp, O., aan de Brugh, J., Schneider, A., Wu, L., Hase, F., Kivi, R., Wunch, D., Pollard, D. F., Shiomi, K., Deutscher, N. M., Velazco, V. A., Roehl, C. M., Wennberg, P. O., Warneke, T., and Landgraf, J.: Methane retrieved from TROPOMI: improvement of the data product and validation of the first 2 years of measurements, *Atmospheric Measurement Techniques*, 14, 665–684, <https://doi.org/10.5194/amt-14-665-2021>, 2021.

Lu, X., Jacob, D. J., Zhang, Y., Maasakkers, J. D., Sulprizio, M. P., Shen, L., Qu, Z., Scarpelli, T. R., Nesser, H., Yantosca, R. M., Sheng, J., Andrews, A., Parker, R. J., Boesch, H., Anthony Bloom, A., and Ma, S.: Global methane budget and trend, 2010–2017: Complementarity of inverse analyses using in situ (globalviewplus ch4 obspack) and satellite (gosat) observations, *Atmospheric Chemistry and Physics*, 21, <https://doi.org/10.5194/acp-21-4637-2021>, 2021.

Lu, X., Jacob, D. J., Wang, H., Maasakkers, J. D., Zhang, Y., Scarpelli, T. R., Shen, L., Qu, Z., Sulprizio, M. P., Nesser, H., Bloom, A. A., Ma, S., Worden, J. R., Fan, S., Parker, R. J., Boesch, H., Gautam, R., Gordon, D., Moran, M. D., Reuland, F., Villasana, C. A. O., and Andrews, A.: Methane emissions in the United States, Canada, and Mexico: evaluation of national methane emission inventories and 2010–2017 sectoral trends by inverse analysis of in situ (GLOBALVIEWplus CH<sub>4</sub> ObsPack) and satellite (GOSAT) atmospheric observations, *Atmos. Chem. Phys.*, 22, 395–418, <https://doi.org/10.5194/acp-22-395-2022>, 2022.

Lu, X., Jacob, D. J., Zhang, Y., Shen, L., Sulprizio, M. P., Maasakkers, J. D., Varon, D. J., Qu, Z., Chen, Z., Hmiel, B., Parker, R. J., Boesch, H., Wang, H., He, C., and Fan, S.: Observation-derived 2010–2019 trends in methane emissions and intensities from US oil and gas fields tied to activity metrics, *Proceedings of the National Academy of Sciences*, 120, e2217900120, <https://doi.org/10.1073/pnas.2217900120>, 2023.

Lucchesi, R.: File Specification for GEOS-5 FP., GMAO Office Note No. 4 (Version 1.1), 61, 2017.

Ma, S., Worden, J. R., Bloom, A. A., Zhang, Y., Poulter, B., Cusworth, D. H., Yin, Y., Pandey, S., Maasakkers, J. D., Lu, X., Shen, L., Sheng, J., Frankenberg, C., Miller, C. E., and Jacob, D. J.: Satellite Constraints on the Latitudinal Distribution and Temperature Sensitivity of Wetland Methane Emissions, *AGU Advances*, 2, <https://doi.org/10.1029/2021AV000408>, 2021.

Maasakkers, J. D., Jacob, D. J., Sulprizio, M. P., Turner, A. J., Weitz, M., Wirth, T., Hight, C., DeFigueiredo, M., Desai, M., Schmeltz, R., Hockstad, L., Bloom, A. A., Bowman, K. W., Jeong, S., and Fischer, M. L.: Gridded National Inventory of U.S. Methane Emissions, *Environmental Science and Technology*, 50, 13123–13133, <https://doi.org/10.1021/acs.est.6b02878>, 2016.

Maasakkers, J. D., Jacob, D. J., Sulprizio, M. P., Scarpelli, T. R., Nesser, H., Sheng, J. X., Zhang, Y., Hersher, M., Anthony Bloom, A., Bowman, K. W., Worden, J. R., Janssens-Maenhout, G., and Parker, R. J.: Global distribution of methane emissions, emission trends, and OH concentrations and trends inferred from an inversion of GOSAT satellite data for 2010–2015, *Atmospheric Chemistry and Physics*, 19, 7859–7881, <https://doi.org/10.5194/acp-19-7859-2019>, 2019.

Maasakkers, J. D., Jacob, D. J., Sulprizio, M. P., Scarpelli, T. R., Nesser, H., Sheng, J., Zhang, Y., Lu, X., Anthony Bloom, A., Bowman, K. W., Worden, J. R., and J. Parker, R.: 2010–2015 North American methane emissions, sectoral contributions, and trends: A high-resolution inversion of GOSAT observations of atmospheric methane, *Atmospheric Chemistry and Physics*, 21, <https://doi.org/10.5194/acp-21-4339-2021>, 2021.

McNorton, J., Bouserez, N., Agustí-Panareda, A., Balsamo, G., Cantarello, L., Engelen, R., Huijnen, V., Inness, A., Kipling, Z., Parrington, M., and Ribas, R.: Quantification of methane emissions from hotspots and during COVID-19 using a global atmospheric inversion, *Atmospheric Chemistry and Physics*, 22, 5961–5981, <https://doi.org/10.5194/acp-22-5961-2022>, 2022.

Miller, S. M., Wofsy, S. C., Michalak, A. M., Kort, E. A., Andrews, A. E., Biraud, S. C., Dlugokencky, E. J., Eluszkiewicz, J., Fischer, M. L., Janssens-Maenhout, G., Miller, B. R., Miller, J. B., Montzka, S. A., Nehrkorn, T., and Sweeney, C.: Anthropogenic emissions of methane in the United States, *Proceedings of the National Academy of Sciences*, 110, 20018–20022, <https://doi.org/10.1073/pnas.1314392110>, 2013.

Miller, S. M., Miller, C. E., Commane, R., Chang, R. Y.-W., Dinardo, S. J., Henderson, J. M., Karion, A., Lindaas, J., Melton, J. R., Miller, J. B., Sweeney, C., Wofsy, S. C., and Michalak, A. M.: A multiyear estimate of methane fluxes in Alaska from CARVE atmospheric observations, *Global Biogeochemical Cycles*, 30, 1441–1453, <https://doi.org/10.1002/2016GB005419>, 2016.

Moore, D. P., Li, N. P., Wendt, L. P., Castañeda, S. R., Falinski, M. M., Zhu, J.-J., Song, C., Ren, Z. J., and Zondlo, M. A.: Underestimation of Sector-Wide Methane Emissions from United States Wastewater Treatment, *Environ. Sci. Technol.*, 57, 4082–4090, <https://doi.org/10.1021/acs.est.2c05373>, 2023.

NAS: Improving Characterization of Anthropogenic Methane Emissions in the United States, The National Academies Press, Washington, D.C., 2018.

Nesser, H., Jacob, D. J., Maasakkers, J. D., Scarpelli, T. R., Sulprizio, M. P., Zhang, Y., and Rycroft, C. H.: Reduced-cost construction of Jacobian matrices for high-resolution inversions of satellite observations of atmospheric composition, *Atmospheric Measurement Techniques*, 14, <https://doi.org/10.5194/amt-14-5521-2021>, 2021.

Pennsylvania DEP: 2022 Pennsylvania Greenhouse Gas Inventory Report, Pennsylvania Department of Environmental Protection, 2022.

Pitt, J. R., Lopez-Coto, I., Hajny, K. D., Tomlin, J., Kaeser, R., Jayarathne, T., Stirm, B. H., Floerchinger, C. R., Loughner, C. P., Gately, C. K., Hutyra, L. R., Gurney, K. R., Roest, G. S., Liang, J., Gourdji, S., Karion, A., Whetstone, J. R., and Shepson, P. B.: New York City greenhouse gas emissions estimated with inverse modeling of aircraft measurements, *Elementa: Science of the Anthropocene*, 10, 00082, <https://doi.org/10.1525/elementa.2021.00082>, 2022.

Plant, G., Kort, E. A., Floerchinger, C., Gvakharia, A., Vimont, I., and Sweeney, C.: Large Fugitive Methane Emissions From Urban Centers Along the U.S. East Coast, *Geophysical Research Letters*, 46, 8500–8507, <https://doi.org/10.1029/2019GL082635>, 2019.

Plant, G., Kort, E. A., Murray, L. T., Maasakkers, J. D., and Aben, I.: Evaluating urban methane emissions from space using TROPOMI methane and carbon monoxide observations, *Remote Sensing of Environment*, 268, 112756, <https://doi.org/10.1016/j.rse.2021.112756>, 2022.

Qu, Z., Jacob, D. J., Shen, L., Lu, X., Zhang, Y., Scarpelli, T. R., Nesser, H., Sulprizio, M. P., Maasakkers, J. D., Bloom, A. A., Worden, J. R., Parker, R. J., and Delgado, A. L.: Global distribution of methane emissions: a comparative inverse analysis of observations from the TROPOMI and GOSAT satellite instruments, *Atmospheric Chemistry and Physics*, 21, 14159–14175, <https://doi.org/10.5194/acp-21-14159-2021>, 2021.

Rodgers, C. D.: *Inverse Methods for Atmospheric Sounding: Theory and Practice*, 2000.

Russell, J.: South Side Landfill planning \$25 million methane-conversion project, Indianapolis Business Journal, 19th March, 2019.

- 965 Sargent, M. R., Floerchinger, C., McKain, K., Budney, J., Gottlieb, E. W., Hutyra, L. R., Rudek, J., and Wofsy, S. C.: Majority of US urban natural gas emissions unaccounted for in inventories, *Proceedings of the National Academy of Sciences*, 118, e2105804118, <https://doi.org/10.1073/pnas.2105804118>, 2021.
- 970 Scarpelli, T. R., Jacob, D. J., Villasana, C. A. O., Hernández, I. F. R., Moreno, P. R. C., Alfaro, E. A. C., García, M. Á. G., and Zavala-Araiza, D.: A gridded inventory of anthropogenic methane emissions from Mexico based on Mexico's national inventory of greenhouse gases and compounds, *Environ. Res. Lett.*, 15, 105015, <https://doi.org/10.1088/1748-9326/abb42b>, 2020.
- Scarpelli, T. R., Jacob, D. J., Moran, M., Reuland, F., and Gordon, D.: A gridded inventory of Canada's anthropogenic methane emissions, *Environ. Res. Lett.*, 17, 014007, <https://doi.org/10.1088/1748-9326/ac40b1>, 2021.
- 975 Schneising, O., Buchwitz, M., Reuter, M., Vanselow, S., Bovensmann, H., and Burrows, J. P.: Remote sensing of methane leakage from natural gas and petroleum systems revisited, *Atmospheric Chemistry and Physics*, 20, 9169–9182, <https://doi.org/10.5194/acp-20-9169-2020>, 2020.
- Seto, K. C., Güneralp, B., and Hutyra, L. R.: Global forecasts of urban expansion to 2030 and direct impacts on biodiversity and carbon pools, *Proceedings of the National Academy of Sciences*, 109, 16083–16088, <https://doi.org/10.1073/pnas.1211658109>, 2012.
- 980 Shen, L., Gautam, R., Omara, M., Zavala-Araiza, D., Maasakkers, J. D., Scarpelli, T. R., Lorente, A., Lyon, D., Sheng, J., Varon, D. J., Nesser, H., Qu, Z., Lu, X., Sulprizio, M. P., Hamburg, S. P., and Jacob, D. J.: Satellite quantification of oil and natural gas methane emissions in the US and Canada including contributions from individual basins, *Atmospheric Chemistry and Physics*, 22, 11203–11215, <https://doi.org/10.5194/acp-22-11203-2022>, 2022.
- Smith, M.: Airborne methane emissions measurement survey: Final summary report, California Air Resources Board, 2021.
- 985 Song, C., Zhu, J.-J., Willis, J. L., Moore, D. P., Zondlo, M. A., and Ren, Z. J.: Methane Emissions from Municipal Wastewater Collection and Treatment Systems, *Environ. Sci. Technol.*, 57, 2248–2261, <https://doi.org/10.1021/acs.est.2c04388>, 2023.
- Spokas, K., Bogner, J., Corcoran, M., and Walker, S.: From California dreaming to California data: Challenging historic models for landfill CH<sub>4</sub> emissions, *Elementa: Science of the Anthropocene*, 3, 000051, <https://doi.org/10.12952/journal.elementa.000051>, 2015.
- 990 Streets, D. G., Canty, T., Carmichael, G. R., De Foy, B., Dickerson, R. R., Duncan, B. N., Edwards, D. P., Haynes, J. A., Henze, D. K., Houyoux, M. R., Jacob, D. J., Krotkov, N. A., Lamsal, L. N., Liu, Y., Lu, Z., Martin, R. V., Pfister, G. G., Pinder, R. W., Salawitch, R. J., and Wecht, K. J.: Emissions estimation from satellite retrievals: A review of current capability, *Atmospheric Environment*, 77, 1011–1042, <https://doi.org/10.1016/j.atmosenv.2013.05.051>, 2013.
- Taylor, T.: Colorado 2021 Greenhouse Gas Inventory Update: With Historical Emissions from 2005 to 2019 and Projections to 2050, Colorado Air Pollution Control Division, Department of Public Health & Environment, 2021.
- 995 The White House: U.S. Methane Emissions Reduction Action Plan: Critical and commonsense steps to cut pollution and consumer costs, while boosting good-paying jobs and American competitiveness, The White House Office of Domestic Climate Policy, 2021.
- Turner, A. J., Jacob, D. J., Wecht, K. J., Maasakkers, J. D., Lundgren, E., Andrews, A. E., Biraud, S. C., Boesch, H., Bowman, K. W., Deutscher, N. M., Dubey, M. K., Griffith, D. W. T., Hase, F., Kuze, A., Notholt, J., Ohyama, H., Parker, R., Payne, V.

H., Sussmann, R., Sweeney, C., Velazco, V. A., Warneke, T., Wennberg, P. O., and Wunch, D.: Estimating global and North American methane emissions with high spatial resolution using GOSAT satellite data, *Atmospheric Chemistry and Physics*, 15, 7049–7069, <https://doi.org/10.5194/acp-15-7049-2015>, 2015.

U.S. Census Bureau: 2010 Census Urban and Rural Classification and Urban Area Criteria, 2010.

1005 U.S. Census Bureau: TIGER/Line Shapefile, 2017, 2010 nation, U.S., 2010 Census Urban Area National, U.S. Census Bureau, 2017.

USDA: 2017 Census of Agriculture, U.S. Department of Agriculture, 2019.

1010 Varon, D. J., Jacob, D. J., Hmiel, B., Gautam, R., Lyon, D. R., Omara, M., Sulprizio, M., Shen, L., Pendergrass, D., Nesser, H., Qu, Z., Barkley, Z. R., Miles, N. L., Richardson, S. J., Davis, K. J., Pandey, S., Lu, X., Lorente, A., Borsdorff, T., Maasakkers, J. D., and Aben, I.: Continuous weekly monitoring of methane emissions from the Permian Basin by inversion of TROPOMI satellite observations, *Atmospheric Chemistry and Physics Discussions*, 1–26, <https://doi.org/10.5194/acp-2022-749>, 2022.

1015 Veefkind, J. P., Aben, I., McMullan, K., Förster, H., de Vries, J., Otter, G., Claas, J., Eskes, H. J., de Haan, J. F., Kleipool, Q., van Weele, M., Hasekamp, O., Hoogeveen, R., Landgraf, J., Snel, R., Tol, P., Ingmann, P., Voors, R., Kruizinga, B., Vink, R., Visser, H., and Levelt, P. F.: TROPOMI on the ESA Sentinel-5 Precursor: A GMES mission for global observations of the atmospheric composition for climate, air quality and ozone layer applications, *Remote Sensing of Environment*, 120, 70–83, <https://doi.org/10.1016/j.rse.2011.09.027>, 2012.

Vera, A.: State finds violations at landfill, *The Progress Index*, 3rd January, 2016.

1020 Wecht, K. J., Jacob, D. J., Frankenberg, C., Jiang, Z., and Blake, D. R.: Mapping of North American methane emissions with high spatial resolution by inversion of SCIAMACHY satellite data, *J. Geophys. Res. Atmos. Res.*, 119, 7741–7756, <https://doi.org/10.1002/2014JD021551>, 2014a.

1025 Wecht, K. J., Jacob, D. J., Sulprizio, M. P., Santoni, G. W., Wofsy, S. C., Parker, R., Bösch, H., and Worden, J.: Spatially resolving methane emissions in California: constraints from the CalNex aircraft campaign and from present (GOSAT, TES) and future (TROPOMI, geostationary) satellite observations, *Atmospheric Chemistry and Physics*, 14, 8173–8184, <https://doi.org/10.5194/acp-14-8173-2014>, 2014b.

Wise, J.: Government Oversight: A review of Dothan's attempts to expand its landfill, *Dothan Eagle*, 27th January, 2019.

Wong, K. W., Fu, D., Pongetti, T. J., Newman, S., Kort, E. A., Duren, R., Hsu, Y.-K., Miller, C. E., Yung, Y. L., and Sander, S. P.: Mapping CH<sub>4</sub> : CO<sub>2</sub> ratios in Los Angeles with CLARS-FTS from Mount Wilson, California, *Atmospheric Chemistry and Physics*, 15, 241–252, <https://doi.org/10.5194/acp-15-241-2015>, 2015.

1030 Worden, J. R., Cusworth, D. H., Qu, Z., Yin, Y., Zhang, Y., Bloom, A. A., Ma, S., Byrne, B. K., Scarpelli, T., Maasakkers, J. D., Crisp, D., Duren, R., and Jacob, D. J.: The 2019 methane budget and uncertainties at 1° resolution and each country through Bayesian integration Of GOSAT total column methane data and a priori inventory estimates, *Atmospheric Chemistry and Physics*, 22, 6811–6841, <https://doi.org/10.5194/acp-22-6811-2022>, 2022.

1035 Wunch, D., Wennberg, P. O., Toon, G. C., Connor, B. J., Fisher, B., Osterman, G. B., Frankenberg, C., Mandrake, L., O'Dell, C., Ahonen, P., Biraud, S. C., Castano, R., Cressie, N., Crisp, D., Deutscher, N. M., Eldering, A., Fisher, M. L., Griffith, D. W. T., Gunson, M., Heikkinen, P., Keppel-Aleks, G., Kyrö, E., Lindenmaier, R., Macatangay, R., Mendonca, J., Messerschmidt, J., Miller, C. E., Morino, I., Notholt, J., Oyafuso, F. A., Rettinger, M., Robinson, J., Roehl, C. M., Salawitch, R. J., Sherlock, V., Strong, K., Sussmann, R., Tanaka, T., Thompson, D. R., Uchino, O., Warneke, T., and Wofsy, S. C.: A

method for evaluating bias in global measurements of CO<sub>2</sub> total columns from space, *Atmospheric Chemistry and Physics*, 11, 1040 12317–12337, <https://doi.org/10.5194/acp-11-12317-2011>, 2011.

Wunch, D., Toon, G. C., Hedelius, J. K., Vizenor, N., Roehl, C. M., Saad, K. M., Blavier, J.-F. L., Blake, D. R., and Wennberg, P. O.: Quantifying the loss of processed natural gas within California's South Coast Air Basin using long-term measurements of ethane and methane, *Atmos. Chem. Phys.*, 16, 14091–14105, <https://doi.org/10.5194/acp-16-14091-2016>, 2016.

Yadav, V., Duren, R., Mueller, K., Verhulst, K. R., Nehrkorn, T., Kim, J., Weiss, R. F., Keeling, R., Sander, S., Fischer, M. L., Newman, S., Falk, M., Kuwayama, T., Hopkins, F., Rafiq, T., Whetstone, J., and Miller, C.: Spatio-temporally Resolved Methane Fluxes From the Los Angeles Megacity, *Journal of Geophysical Research: Atmospheres*, 124, 5131–5148, <https://doi.org/10.1029/2018JD030062>, 2019.

Yadav, V., Verhulst, K., Duren, R., Thorpe, A., Kim, J., Keeling, R., Weiss, R., Cusworth, D., Mountain, M., Miller, C., and Whetstone, J.: A declining trend of methane emissions in the Los Angeles basin from 2015 to 2020, *Environ. Res. Lett.*, 18, 1050 034004, <https://doi.org/10.1088/1748-9326/acb6a9>, 2023.

Yu, X., Millet, D. B., Wells, K. C., Henze, D. K., Cao, H., Griffis, T. J., Kort, E. A., Plant, G., Deventer, M. J., Kolka, R. K., Roman, D. T., Davis, K. J., Desai, A. R., Baier, B. C., McKain, K., Czarnetzki, A. C., and Bloom, A. A.: Aircraft-based inversions quantify the importance of wetlands and livestock for Upper Midwest methane emissions, *Atmospheric Chemistry and Physics*, 21, 951–971, <https://doi.org/10.5194/acp-21-951-2021>, 2021.

Zhang, Y., Jacob, D. J., Maasakkers, J. D., Sulprizio, M. P., Sheng, J.-X., Gautam, R., and Worden, J.: Monitoring global tropospheric OH concentrations using satellite observations of atmospheric methane, *Atmospheric Chemistry and Physics*, 18, 15959–15973, <https://doi.org/10.5194/acp-18-15959-2018>, 2018.

Zhang, Y., Gautam, R., Pandey, S., Omara, M., Maasakkers, J. D., Sadavarte, P., Lyon, D., Nesser, H., Sulprizio, M. P., Varon, D. J., Zhang, R., Houweling, S., Zavala-Araiza, D., Alvarez, R. A., Lorente, A., Hamburg, S. P., Aben, I., and Jacob, D. J.: Quantifying methane emissions from the largest oil-producing basin in the United States from space, *Science Advances*, 6, eaaz5120, <https://doi.org/10.1126/sciadv.aaz5120>, 2020.